Yoder, A. J., Walsh, C. P. & Bestor, T. H. 1997. Cytosine methylation and the ecology of intragenomic parasites. *Trends Genet.* **13**, 335–340.

Yoo, C. B. & Jones, P. A. 2006. Epigenetic therapy of cancer: past, present and future. *Nat. Rev. Drug Discov.* **5**, 37–50.

Yoon, K. J., Koo, B. K., Im, S. K., Jeong, H. W., Ghim, J., Kwon, M. C., Moon, J. S., Miyata, T. & Kong, Y. Y. 2008. Mind bomb 1-expressing intermediate progenitors generate notch signaling to maintain radial glial cells. *Neuron* **58**, 519–531.

Zhao, C., Sun, G., Li, S. & Shi, Y. 2009. A feedback regulatory loop involving microRNA-9 and nuclear receptor TLX in neural stem cell fate determination. *Nat. Struct. Mol. Biol.* **16**, 365–371.

Zhao, X., Ueba, T., Christie, B. R., Barkho, B., McConnell, M. J., Nakashima, K., Lein, E. S., Eadie, B. D., Willhoite, A. R., Muotri, A. R., Summers, R. G., Chun, J., Lee, K. F. & Gage, F. H. 2003. Mice lacking methyl-CpG binding protein 1 have deficits in adult neurogenesis and hippocampal function. *Proc. Natl Acad. Sci. USA* **100**, 6777–6782.

Development 137, 1515-1522 (2010) doi:10.1242/dev.044545

The oscillation of Notch activation, but not its boundary, is required for somite border formation and rostral-caudal patterning within a somite

Masayuki Oginuma[1,2,*], Yu Takahashi[3,*], Satoshi Kitajima[3], Makoto Kiso[2], Jun Kanno[3], Akatsuki Kimura[1,4] and Yumiko Saga[1,2,†]

SUMMARY

Notch signaling exerts multiple roles during different steps of mouse somitogenesis. We have previously shown that segmental boundaries are formed at the interface of the Notch activity boundary, suggesting the importance of the Notch on/off state for boundary formation. However, a recent study has shown that mouse embryos expressing Notch-intracellular domain (NICD) throughout the presomitic mesoderm (PSM) can still form more than ten somites, indicating that the NICD on/off state is dispensable for boundary formation. To clarify this discrepancy in our current study, we created a transgenic mouse lacking NICD boundaries in the anterior PSM but retaining Notch signal oscillation in the posterior PSM by manipulating the expression pattern of a Notch modulator, lunatic fringe. In this mouse, clearly segmented somites are continuously generated, indicating that the NICD on/off state is unnecessary for somite boundary formation. Surprisingly, this mouse also showed a normal rostral-caudal compartment within a somite, conferred by a normal Mesp2 expression pattern with a rostral-caudal gradient. To explore the establishment of normal Mesp2 expression, we performed computer simulations, which revealed that oscillating Notch signaling induces not only the periodic activation of *Mesp2* but also a rostral-caudal gradient of Mesp2 in the absence of striped Notch activity in the anterior PSM. In conclusion, we propose a novel function of Notch signaling, in which a progressive oscillating wave of Notch activity is translated into the rostral-caudal polarity of a somite by regulating *Mesp2* expression in the anterior PSM. This indicates that the initial somite pattern can be defined as a direct output of the segmentation clock.

KEY WORDS: Notch signaling, Hes7, Mesp2, Segmentation clock, Presomitic mesoderm, Lunatic fringe, Somitogenesis

INTRODUCTION

The periodicity of the segmented somites is established in the posterior presomitic mesoderm (PSM) via the function of a so-called molecular clock, which is based on complex gene regulatory networks under the control of three major signaling pathways: Notch, Fgf and Wnt (Dequeant et al., 2006; Dequeant and Pourquie, 2008). Among these pathways, Fgf and Wnt are implicated in the maintenance of immature PSM cells (Aulehla et al., 2003; Aulehla et al., 2008; Wahl et al., 2007; Delfini et al., 2005; Niwa et al., 2007), whereas Notch signaling might be directly involved in the generation of periodicity (Oginuma et al., 2008; Yasuhiko et al., 2006; Takahashi et al., 2000; Takahashi et al., 2003). In mice, Notch signal oscillations are produced by the suppressive function of the glycosyltransferase lunatic fringe (Lfng) as the levels of activated Notch1 (cleaved form of the Notch1 intracellular domain, referred to as cNICD hereafter) are upregulated in the *Lfng*-null mouse embryo (Morimoto et al., 2005). The expression of *Lfng* exhibits a biphasic pattern involving oscillation in the posterior PSM and a stabilized striped pattern in the anterior PSM (Aulehla and Johnson, 1999; McGrew et al., 1998; Morales et al., 2002; Cole et al., 2002). The oscillatory expression of *Lfng* is positively regulated by Notch signaling as it is greatly downregulated in *Dll1*-null mice, whereas it is negatively regulated by Hes7 as revealed by its upregulation in *Hes7*-null embryos (Barrantes et al., 1999; Bessho et al., 2003; Morales et al., 2002). The stabilized expression of *Lfng* is under the control of the Mesp2 transcription factor and stabilization does not occur in the absence of Mesp2 (Morimoto et al., 2005). In the absence of Lfng, no clear segmental border is defined and the rostral-caudal (R-C) compartmentalization within a somite is randomized (Zhang and Gridley, 1998; Evrard et al., 1998).

In the anterior PSM, the Mesp2 transcription factor plays an important role in the creation of a cNICD on/off state that corresponds to the future segmental boundary via the activation of Lfng transcription (Morimoto et al., 2005). This suggests that the Notch on/off state is important for boundary formation. However, a recent study has shown that mouse embryos expressing Notch activity throughout the PSM still show the ability to form more than ten somites, indicating that the Notch on/off state is dispensable for boundary formation (Feller et al., 2008). By contrast, however, other studies have reported that transgenic mice expressing *Lfng* only in the anterior PSM show normal segmental border formation after embryonic day 10.5 (E10.5), suggesting that the Notch on-off state generated in the anterior PSM is sufficient to create a somite boundary at least in the later stage embryos (Shifley et al., 2008; Stauber et al., 2009).

To resolve this discrepancy, we have, in our current study, generated a mouse that lacks the anterior striped Lfng expression pattern, but at the same time retains oscillating Lfng activity in the

[1]Department of Genetics, SOKENDAI, 1111 Yata, Mishima, Shizuoka 411-8540, Japan. [2]Division of Mammalian Development, National Institute of Genetics, Yata 1111, Mishima 411-8540, Japan. [3]Division of Cellular and Molecular Toxicology, National Institute of Health Sciences, 1-18-1 Kamiyoga, Setagaya-ku, Tokyo 158-8501, Japan. [4]Cell Architecture Laboratory, National Institute of Genetics, Yata 1111, Mishima 411-8540, Japan.

*These authors contributed equally to this work
†Author for correspondence (ysaga@lab.nig.ac.jp)

Accepted 17 February 2010

posterior PSM. The resulting transgenic mouse shows no clear cNICD on/off state in the anterior PSM. Nevertheless, this mouse exhibits normal boundary formation, indicating that the cNICD boundary is dispensable for somite formation. In addition, our transgenic mouse shows normal R-C patterning within a somite. Further analyses by computer simulation have led us to conclude that Notch signaling oscillation functions as an output signal that is both required and sufficient to establish the *Mesp2* expression pattern needed for normal somitogenesis.

MATERIALS AND METHODS

Animals

The wild-type mice used in this study were the MCH strain (a closed colony established at CLEA, Japan). The *Lfng*-null (Evrard et al., 1998), *Mesp2*-null (*Mesp2*$^{MCM/+}$) (Takahashi et al., 2007) and *Mesp2-lacZ* (*Mesp2*$^{lacZ/+}$) (Takahashi et al., 2000) mouse lines are maintained in the animal facility of the National Institute of Genetics and National Institute of Health Sciences, Japan.

Gene targeting strategy to generate the *Mesp2*^{Lfng} allele

The knock-in strategy used to target the *Mesp2* locus is largely similar to our previously described method (Takahashi et al., 2000), except that *Lfng* cDNA was inserted. The *pgk-neo* cassette flanked by a *lox* sequence was removed by crossing with *CAG-Cre* mice (Sakai and Miyazaki, 1997).

Generation of the *Hes7-Lfng* transgenic mice

We used a 12 kb *Hes7* gene cassette comprising 5 kb of upstream sequence and all of the exons and introns, as this construct had previously been confirmed to be sufficient to reproduce the endogenous *Hes7* oscillation pattern when inserted in-frame at the translational start site (Kageyama et al., personal communications). We generated the construct *Lfng IRES-EGFP*, in which *IRES* (internal ribosomal entry site)-*EGFP* (enhanced GFP) was fused to the 3′ end of *Lfng* cDNA, and inserted this construct into the *Hes7*-translational initiation site. The resulting DNA was digested with restriction enzymes to remove vector sequences and gel purified. Transgenic mice were generated by microinjection of this construct into fertilized eggs, which were then transferred into the oviducts of pseudopregnant foster females.

In situ hybridization, immunohistochemistry, histology and skeletal preparations

The methods used for wholemount in situ hybridization, section in situ hybridization, immunohistochemistry, histology and skeletal preparation by Alcian Blue/Alizarin Red staining are described in our previous reports (Morimoto et al., 2005; Oginuma et al., 2008; Takahashi et al., 2000). The cNICD signal was detected by immunohistochemistry using anti-cleaved NICD (Val1744; 1:500; Cell Signaling Technology). Probes were prepared also as described previously: *Mesp2* exon-intron (Oginuma et al., 2008), *Mesp2* (Takahashi et al., 2000) and *Lfng* (Evrard et al., 1998). The *GFP* cRNA probe was prepared by PCR-amplification of *GFP* cDNA.

Computer simulation

Our computer simulation model is based on the previous mathematical description of a clock-and-wavefront model constructed by J. Lewis (Palmeirim et al., 1997). By using the basic oscillating function in the Lewis model, we modeled the activity of cNICD, n, at given time, t, and anteroposterior position, x, as:

$$n(x,t)=\left[1-\cos\left\{2\pi\int_0^t\frac{1}{1+e^{(x+t)/2}}dt\right\}\right]/2 .$$

For the control simulation with constant activity of cNICD, the cNICD activity, n, was set to 0.3. For the simulation with oscillating cNICD without wave, n was formulated as $n(x,t)=\{1-\cos(\pi t)\}/2$. The activity of Fgf8 is known to gradually decrease from posterior to anterior, and also according to the time elapsed. These features of Fgf8 fit well with the formulation of the clock cycling rate in the Lewis model and, thus, we calculated the activity of Fgf8, f, using the formula $f(x,t)=1/(1+e^{(x+t)/2})$.

We next added the regulation of Mesp2 and Tbx6 expression to the model. As cNICD and Fgf8 play positive and negative roles for *Mesp2* expression, respectively, we assumed that the increase of *Mesp2* expression occurs when the cNICD activity, n, exceeds that of Fgf8, f, with the amount dependent on n–f. Tbx6 (b) is also required for *Mesp2* expression. We thus modeled the *Mesp2* mRNA expression, m, and Mesp2 protein expression, p, as:

$$m(x,t+\Delta t)=m(x,t)+S_m\times\frac{[\{n(x,t)-f(x,t)\}/K_n]^{H_n}}{1+[\{n(x,t)-f(x,t)\}/K_n]^{H_n}}\times\frac{\{b(x,t)/K_b\}^{H_b}}{1+\{b(x,t)/K_b\}^{H_b}}-D_m\times m(x,t),$$

$$p(x,t+\Delta t)=p(x,t)+S_p\times m(x,t-T)-D_p\times p(x,t),$$

with the initial condition $m(x,0)=0$, and $p(x,0)=0$. The degradation of Tbx6 is dependent on Mesp2 (Oginuma et al., 2008). We introduced a hypothetical molecule, z, that is expressed depending on Mesp2 and degrades Tbx6 by interacting with it. The expression of Tbx6 (b) and the Tbx6 degrading molecule (z) were modeled as:

$$z(x,t+\Delta t)=z(x,t)+S_z\times\frac{\{p(x,t-T)/K_p\}^{H_p}}{1+\{p(x,t-T)/K_p\}^{H_p}}-D_z\times z(x,t),$$

$$b(x,t+\Delta t)=b(x,t)-D_b\times\{b(x,t)\}^{Bb}\times\{z(x,t)\}^{Bz},$$

with the initial condition $z(x,0)=0$, and $b(x,0)=1.0$.

These formulas were implemented using C language. The activities of cNICD (n), Fgf8 (f), Mesp2 (m and p), Tbx6-regulator (z) and Tbx6 (b) were calculated over the ranges $-12.5\leq x\leq -2.5$ and $0\leq t\leq 20$. The calculations were conducted discretely with a single unit of x (Δx) of 1/10 and t (Δt) of 1/10. The parameter values we used are shown in Table S1 in the supplementary material. We also introduced time delay, $T=2\Delta t$, for protein expression (Lewis, 2003), which did not affect the results much.

RESULTS

Dissection of the *Lfng* expression pattern in the PSM

To examine the significance of the Notch on/off state during boundary formation, we focused on *Lfng* expression, which exhibits a biphasic pattern involving oscillation in the posterior PSM and a stabilized striped pattern in the anterior PSM (Aulehla and Johnson, 1999; Cole et al., 2002; McGrew et al., 1998; Morales et al., 2002). Each of these two patterns is implicated in the generation of the corresponding Notch activity profile via negative regulation. To induce only the oscillatory expression of *Lfng*, we utilized the *Hes7* transcriptional regulatory unit as the oscillation of *Lfng* and *Hes7* is regulated by similar factors, i.e. positively by Notch signaling and negatively by Hes7 protein. As shown in Fig. 1, these two transcripts show similar expression patterns in the oscillation phase. Both signals manifest a waved pattern within the Tbx6 expression domain from phase I to phase III (Fig. 1A-L). However, in phases I-II, *Hes7* expression is lost from the anterior domain (Fig. 1G-J), whereas that of *Lfng* persists for a longer period in the anterior PSM and forms a clear stripe (Fig. 1A-D,M,O). It should also be noted that the anterior *Lfng* expression domain was found to merge with that of the Mesp2 protein (Fig. 1N,P), the expression of which is restricted to the anterior PSM. This is not unexpected as *Lfng* expression is induced by Mesp2 in the anterior PSM and creates the Notch on/off state (Morimoto et al., 2005). Taken together, we concluded from these data that the *Lfng* expression pattern can be reproduced by two distinct regulatory systems – the *Hes7* promoter-enhancer and the *Mesp2* regulatory system – and this enabled us to further investigate the significance of Notch activities.

The cNICD on/off state is not required for somite boundary formation

To further elucidate the functional significance of the oscillatory cNICD in the posterior PSM and that of the cNICD on/off state in the anterior PSM, we generated a transgenic mouse line by inserting *Lfng* cDNA flanked with *IRES-EGFP* under the control of the Hes7 promoter (see Fig. S1A in the supplementary material). As expected, the expression pattern of this transgene, examined by in situ hybridization using *EGFP* as a probe, was found to be very similar to that of endogenous *Hes7* and *Lfng* except for the lack of anterior striped expression (see Fig. S1B-D in the supplementary material). We then introduced this transgene into the *Lfng*-null genetic background to establish the *Hes7>Lfng/Lfng*$^{-/-}$ mouse line and examined the expression pattern of exogenous *Lfng* and cNICD expression in the absence of endogenous *Lfng* expression (i.e. an *Lfng*-null background). In wild-type embryos, *Lfng* and cNICD showed biphasic patterns, these being oscillation in the posterior PSM and stabilization in the anterior PSM, whereas cNICD oscillation was barely detectable and a constant level of cNICD could be observed through the entire PSM in the absence of *Lfng*, as reported previously (Morimoto et al., 2005). In the *Hes7>Lfng/Lfng*$^{-/-}$ embryo, however, we observed the recovery of cNICD oscillation in the posterior PSM, which overlapped with *Lfng* expression (Fig. 2A-F), clearly indicating that the *Lfng* transgene was functionally active in these embryos. In addition, we previously showed that cNICD and Mesp2 generate a clear boundary in the anterior PSM, which demarcates the presumptive segmental border in phase-II embryos (Morimoto et al., 2005) (Fig. 2G-I). In the absence of *Lfng*, this clear border between cNICD and Mesp2 was not generated and a merged pattern was instead observed

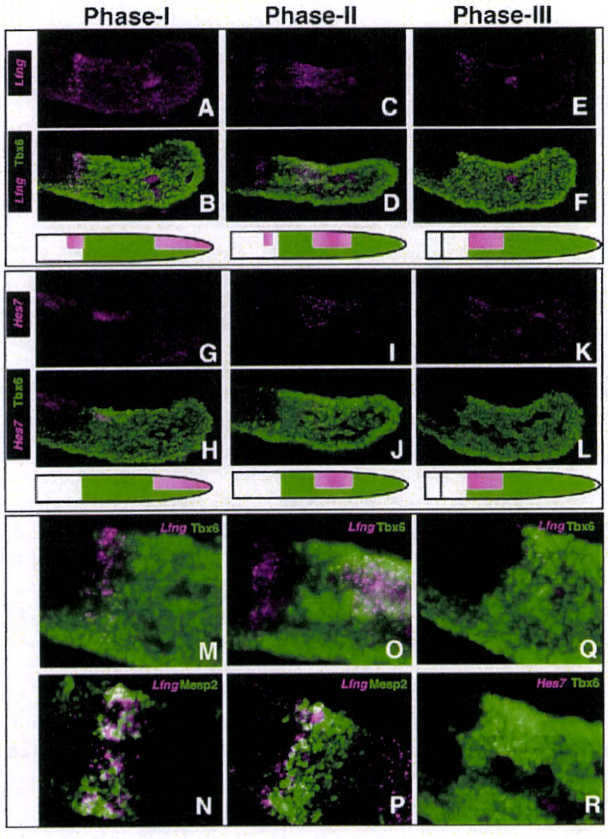

Fig. 1. Comparison of the *Hes7* and *Lfng* expression patterns. In situ hybridization analysis of the spatiotemporal changes in the *Lfng* (**A-F**) and *Hes7* (**G-L**) transcription patterns during somitogenesis by double staining for the Tbx6 protein as the reference point. The stained sections shown in the vertical rows are derived from a single embryo. The phase was defined by the location of the *Hes7* and *Lfng* transcripts and the waves of oscillating *Hes7* and *Lfng* were initiated at the posterior PSM (Phase I). The oscillating wave then moves to the intermediate PSM (Phase II) and reaches the anterior PSM (Phase III). (**M,O,Q,R**) Magnified images of B, D, F and L, respectively. Phase I and Phase II sections were also subjected to double staining for *Lfng* mRNA and Mesp2 (**N,P**).

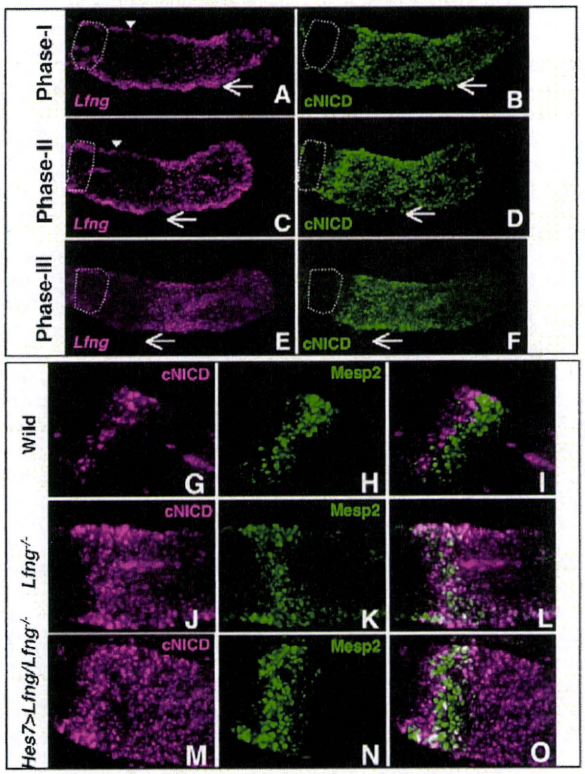

Fig. 2. *Hes7>Lfng/Lfng*$^{-/-}$ mice show cNICD oscillation in the posterior PSM but do not form a cNICD boundary in the anterior PSM. (**A-F**) The patterns of *Lfng* mRNA (A,C,E) and cNICD (B,D,F) expression were revealed in each channel by double staining of these signals using single embryos of *Hes7>Lfng/Lfng*$^{-/-}$ mice at three different phases, I-III, respectively. *Lfng* expression shows a traveling wave (arrow) but no stabilized stripe (arrowheads, A,C). The first somite is indicated by a white dotted line. The wave of oscillating cNICD is initiated at the posterior PSM (B; Phase I; *n*=3), moves to the intermediate PSM (D; Phase II; *n*=4) and eventually reaches the anterior PSM (F; Phase III; *n*=3). (**G-O**) The relationship between cNICD and Mesp2 in Phase II was compared among wild-type (G-I), *Lfng*$^{-/-}$ (J-L) and *Hes7>Lfng/Lfng*$^{-/-}$ (M-O) embryos by double staining. Single channels for cNICD (G,J,M) and Mesp2 (H,K,N), and merged images of both (I,L,O), are shown. In the wild-type embryos, cNICD and Mesp2 generate a clear boundary (I). *Lfng*$^{-/-}$ and *Hes7>Lfng/Lfng*$^{-/-}$ mice, however, do not show a clear segregation between cNICD and Mesp2 (L,O).

(Fig. 2J-L). In the *Hes7>Lfng/Lfng*$^{-/-}$ embryo, as expected by the lack of Lfng expression in the anterior PSM, we did not detect segregation between the cNICD and Mesp2 domains (Fig. 2M-O). *Lfng*$^{-/-}$ embryos did not show clear somite boundaries, although incomplete somites did appear to be formed (see Fig. S2 in the supplementary material), as also suggested previously (Evrard et al., 1998; Zhang and Gridley, 1998). Very surprisingly, however, *Hes7>Lfng/Lfng*$^{-/-}$ embryos showed clearly segmented somites (Fig. 3A-C). This strongly indicates that the oscillatory expression of cNICD mediated via oscillating Lfng is sufficient to provide the conditions for normal somitogenesis to occur and that the cNICD boundary in the anterior PSM is not required for this process.

Recently, we and others have suggested that the Mesp2 downstream events, such as the activation of ephrin-EphA4 signaling and the formation of a Tbx6 protein boundary, were more important for segmental border formation (Watanabe et al., 2009; Oginuma et al., 2008; Nakajima et al., 2006). In *Lfng*$^{-/-}$ embryos, the expression of *EphA4* and the Tbx6 protein boundary were found to be diffuse or randomized (Fig. 3E,J-L), whereas in *Hes7>Lfng/Lfng*$^{-/-}$ embryos, these expression patterns appeared to be normal (Fig. 3F,M-O), i.e. similar to those in wild-type embryos (Fig. 3D,G-I). Taken together, our current findings show that the cNICD boundary is dispensable, but that the Mesp2 boundary might be required, for the creation of the segmental border through the regulation of downstream genes.

R-C polarity is completely recovered in *Hes7>Lfng/Lfng*$^{-/-}$ embryos

We next further examined the morphological features of the *Hes7>Lfng/Lfng*$^{-/-}$ embryo. Surprisingly, these transgenic embryos showed a completely normal skeletal system, with segmented vertebra and ribs (Fig. 4A-C). Furthermore, the expression pattern of *Uncx4.1*, a caudal marker of R-C polarity (Fig. 4D), was fully recovered in the *Hes7>Lfng/Lfng*$^{-/-}$ embryo (Fig. 4F), which contrasts with the randomized pattern we observed in the *Lfng*$^{-/-}$ embryo (Fig. 4E). These results suggest that the cNICD boundary in

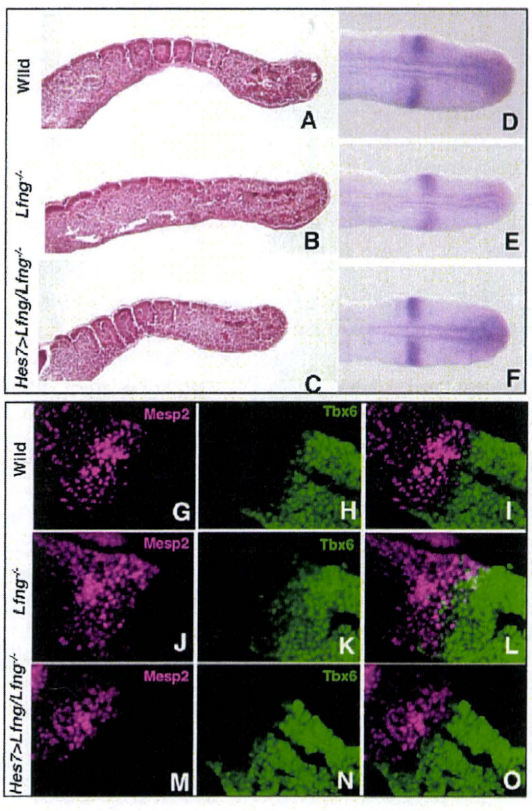

Fig. 3. Exogenous *Lfng* controlled by the *Hes7* promoter completely rescues the boundary formation defect in the *Lfng*$^{-/-}$ mice. The segmental morphologies (**A-C**), the *EphA4* expression pattern (**D-F**) and the relationship between Mesp2 and Tbx6 in Phase II (**G-O**) were compared among wild-type (A,D,G-I), *Lfng*$^{-/-}$ (B,E,J-L) and *Hes7>Lfng/Lfng*$^{-/-}$ (C,F,M-O) using E11.5 embryonic tail regions. Single channels for Mesp2 (G,J,M) and Tbx6 (H,K,N), and merged images of both (I,L,O), are shown. Expression of the *EphA4* and Tbx6 protein boundary forms a clear border in the wild-type (D, *n*=7; G-I, *n*=4) and *Hes7>Lfng/Lfng*$^{-/-}$ embryos (F, *n*=4; M-O, *n*=4), but this is diffuse or randomized in the *Lfng*$^{-/-}$ embryos (E, *n*=4; J-L, *n*=3).

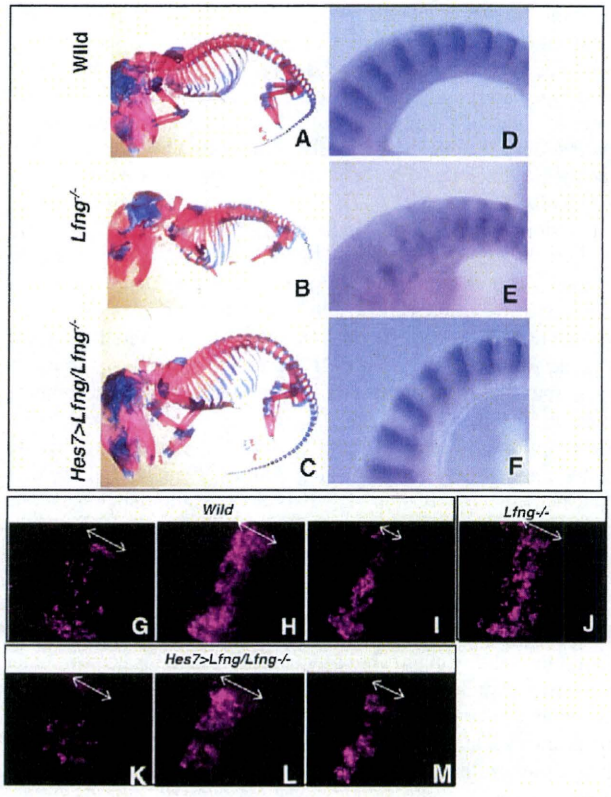

Fig. 4. Exogenous *Lfng* under the control of the *Hes7* promoter completely rescues the R-C patterning defect in the somites of *Lfng*$^{-/-}$ mice. A comparison of the segmental morphologies of skeletal preparations of E17.5 embryos (**A-C**) and the expression pattern of *Uncx4.1*, indicative of R-C patterning within a somite (**D-F**). *Hes7>Lfng/Lfng*$^{-/-}$ mice show a normal skeleton (C, *n*=4) and expression pattern of *Uncx4.1* (F, *n*=3), whereas *Lfng*$^{-/-}$ mice show randomized pattern of skeleton (B) and *Uncx4.1* expression (E). (**G-M**) *Mesp2* transcription states revealed by high resolution in situ hybridization analysis of wild-type embryos for transcriptional initiation (G, *n*=3), active state (H, *n*=5) and rostral localization (I, *n*=3), and *Lfng*-null (J, *n*=11) and *Hes7>Lfng/Lfng*$^{-/-}$ embryos for transcriptional initiation (K, *n*=2), active state (L, *n*=3) and rostral localization (M, *n*=3). Double arrows indicate the length of the *Mesp2* transcription domains.

the anterior PSM is not required for normal R-C polarity patterning. To elucidate this issue further, we focused on the expression of *Mesp2*, which is thought to be the final output signal of the segmentation clock. *Mesp2* is initially expressed over one somite length and then becomes localized in the rostral compartment (Takahashi et al., 2000). This dynamic expression pattern generates a gradient of Mesp2 activity that allows PSM cells to form the R-C pattern within a somite (Takahashi et al., 2003; Takahashi et al., 2000). We therefore next compared the *Mesp2* expression pattern at the cellular level among the wild-type, $Lfng^{-/-}$ and $Hes7{>}Lfng/Lfng^{-/-}$ embryos using high-resolution in situ hybridization. By focusing on the length of the *Mesp2* transcription domain along the A-P axis, we found four distinct patterns in the wild-type embryos: (1) no signal (n=4/15); (2) most cells show nuclear dots indicating transcriptional initiation, and the length of the *Mesp2* transcription domain is approximately 11-13 cells (Fig. 4G; n=3/15); (3) active stage in which signals can be observed in the cytoplasm in addition to nuclear dots, and the length of *Mesp2* transcription is approximately 10-12 cells, with anterior cells showing stronger signals (Fig. 4H; n=5/15); and (4) rostral localization in which the length of the *Mesp2* transcription domain becomes approximately 5-6 cells (Fig. 4I; n=3/15). In contrast to wild-type embryos, only one pattern was observed in the *Lfng*-null embryos: signals were observed in the cytoplasm in addition to nuclear dots, the expression levels were randomized for each cells, and the length of the *Mesp2* transcription domain was approximately 9-11 cells (Fig. 4J; n=11/11). These results indicate that *Mesp2* expression is always present in the anterior PSM without clear on/off cycles in the *Lfng*-null embryo. In addition, the *Mesp2* expression domain is kept to one somite length and there is no clear localization into the rostral compartment, although cellular or cell cluster-level localization might occur in a salt-and-pepper pattern in the absence of Lfng. Importantly, the *Mesp2* expression pattern was found to show four distinct patterns similar to those in wild-type embryos even in the $Hes7{>}Lfng/Lfng^{-/-}$ embryos, i.e. no signal (1/9), transcriptional initiation (Fig. 4K, n=2/9), active stage (Fig. 4L, n=3/9) and rostral localization (Fig. 4M; n=3/9). Our findings thus indicate that the oscillation of cNICD alone is sufficient to generate the normal *Mesp2* expression pattern and that the anterior PSM-specific regulation of cNICD via Lfng is dispensable for this process.

Modeling of the *Mesp2* expression pattern

To test the validity of our above hypothesis, we performed computer simulations. Our model is based on that previously proposed by Lewis and colleagues, in which the oscillatory waves emanate, travel and eventually cease, as it adopts the notion of maturity, which delays the oscillation cycle towards the anterior as time proceeds (Palmeirim et al., 1997). In this model of Lewis, the cessation of the oscillatory waves triggers periodic gene expression along an anterior-posterior direction that leads to the formation of the somites (Palmeirim et al., 1997). In our current study, we applied the Lewis model to the oscillatory waves of the cNICD and assumed Fgf as a molecular basis for maturity. We further incorporated the regulatory network required for *Mesp2* expression, in which cNICD oscillation and Tbx6 synergistically activate (Yasuhiko et al., 2006; Oginuma et al., 2008), whereas the Fgf gradient suppresses *Mesp2* expression and Tbx6 is degraded downstream of Mesp2 (Fig. 5A). Very surprisingly, this simple simulation successfully mimicked some specific features of dynamic *Mesp2* transcription (red line), not only in terms of on/off cycles but also with regard to temporal changes in the expression pattern (from one somite length to rostral localization) along the anterior-posterior axis (Fig. 5B; see Movie 1 in the supplementary material), similar to that observed in vivo (Fig. 4G-I; see Fig. S3A,B in the supplementary material). In addition, this simulation also reproduced the gradient of Mesp2 activity accumulation (black line), which is similar to the *Mesp2*-β-gal pattern we observed in the $Mesp2^{lacZ/+}$ embryos (see Fig. S3E in the supplementary material).

To test the importance of the cNICD wave for the gradient formation of Mesp2 activity, we examined *Mesp2* expression under constant activity of cNICD in the PSM (Fig. 5C; see Movie 2 in the supplementary material). In this instance, *Mesp2* expression is always observed in the anterior PSM without either clear on/off cycles or localization at the rostral compartment, which is very similar to the in vivo situation of the $Lfng^{-/-}$ embryos (Fig. 4J; see Fig. S3C,D,F in the supplementary material). Interestingly, in our model, neither the formation of the waved pattern of cNICD nor its migration is necessary to establish the gradient of Mesp2 activity because a spatially uniform, but temporally oscillating, Notch signaling activity is sufficient to reproduce this gradient (see Fig. S4 and Movie 3 in the supplementary material). Without a traveling wave, however, the temporal transition of the Mesp2 expression pattern from a one-somite length to a rostral localization was not reproduced (see Fig. S4 and Movie 3 in the supplementary material). We thus speculate that this transition might be important for robust somite formation with a correct R-C polarity and propose that the wave of Notch activity enables PSM cells to establish not only the periodic expression of *Mesp2*, but also their localization into the rostral compartment. Our model therefore provides a new concept that indicates that a progressive oscillating wave of Notch activity is translated into the R-C polarity of a somite through the regulation of the Mesp2 expression pattern.

Anterior PSM-specific *Lfng* cannot rescue the defects in *Mesp2*-null or *Lfng*-null mice

Finally, to further ask the significance of the anterior striped cNICD domain for somite boundary formation, we established a mouse line that reproduces this expression pattern by introducing *Lfng* cDNA at the *Mesp2* locus using embryonic stem cell-mediated homologous recombination (see Fig. S1E in the supplementary material). The resulting heterozygous mice showed no abnormalities and we generated an intercross of $Mesp2^{Lfng/+}$ to yield $Mesp2^{Lfng/Lfng}$. In the $Mesp2^{Lfng/Lfng}$ embryos, cNICD signals were suppressed in the *Lfng*-expressing cells in the anterior PSM (Fig. 6B), as seen in the wild type (Fig. 6A). We further found that some of the cells that did not express *Lfng* maintained cNICD signals, indicating that Lfng suppresses cNICD production in a cell-autonomous manner (Fig. 6D). However, Lfng did not rescue the phenotype of the *Mesp2*-null mice (Fig. 6H-M), indicating that the function of *Lfng* downstream of *Mesp2* is not important.

We next introduced this transgene into the *Lfng*-null genetic background to generate a $Mesp2^{Lfng/+}Lfng^{-/-}$ mouse. The expression levels of *Lfng* in the *Mesp2* locus were found to be low (Fig. 6C,E; see Fig. S5C in the supplementary material), but we did observe downregulation of the cNICD signal in the *Mesp2*-expressing cells (Fig. 6F) in comparison with the *Lfng*-null embryos (Fig. 6G). Furthermore, *Hes5* expression (see Fig. S5D in the supplementary material), a target gene of Notch signaling, was severely downregulated in both the $Mesp2^{Lfng/Lfng}$ and $Mesp2^{Lfng/+}Lfng^{-/-}$ embryos (see Fig. S5F,H in the supplementary material) compared with *Mesp2*- and *Lfng*-null embryos (see Fig. S5E,G in the supplementary material), indicating that *Lfng* under the control of *Mesp2* might effectively suppress Notch signaling. However, we did

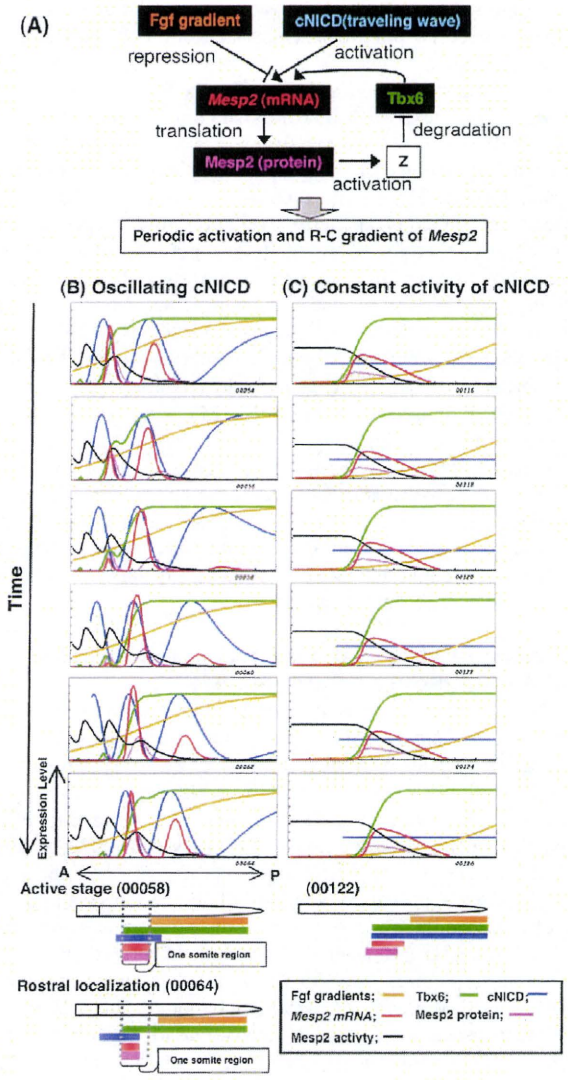

Fig. 5. Model of *Mesp2* expression. (**A**) Schematic representation indicating relationships among *Mesp2* mRNA, Mesp2 protein, Tbx6, cNICD and Fgf signaling, which is used for computer simulation to reproduce the periodic activation and R-C gradient of *Mesp2* expression. z is a hypothetical molecule that functions downstream of Mesp2 and mediates negative-feedback regulation of Tbx6. (**B**,**C**) Expression patterns of *Mesp2*, cNICD and other proteins along the anteroposterior axis predicted in our numerical model. Snapshot images of computer simulations of one cycle of somite formation in the presence (B) or absence (C) of cNICD oscillation are shown. Colored lines indicate levels of cNICD (blue), Fgf8 (orange), *Mesp2* expression (mRNA, red line; protein, pink line) and Tbx6 (green). Mesp2 activity, reflecting the total accumulation of Mesp2 protein, is shown as a tracking line in black. Data sets were taken from Movies 1 (frame 54-64) and 2 (frame 116-126) in the supplementary material, respectively. cNICD (blue) was made to disappear in the panels after one somite is formed, according to experimental observations (Morimoto et al., 2005; Oginuma et al., 2008). Lower diagrams indicate the relationships among these factors at critical time points. Snapshot (00058) corresponds to the transcriptionally active stage of *Mesp2* in which a cNICD wave (blue) reaches the anterior PSM and *Mesp2* (red) is activated in the one-somite region. Snapshot (00064) corresponds to the rostral localization stage, i.e. following the anterior shift of the cNICD wave, the *Mesp2* expression domain also shifts to the rostral region, generating a gradient of Mesp2 activity (black). As the level of cNICD is constant in the *Lfng*-null situation [corresponding to snapshot (00112)], *Mesp2* expression (red) does not show a dynamic pattern and regresses posteriorly.

not detect any significant rescue of the segmental morphology in the developing embryos or of the vertebral morphology at any level along the anteroposterior axis in the $Mesp2^{Lfng/+}Lfng^{-/-}$ mice compared with the *Lfng*-null mouse (Fig. 6N-Q; see Fig. S6 in the supplementary material). These results further confirmed that the suppression of cNICD signaling by stabilized Lfng is not sufficient for normal somitogenesis to occur.

DISCUSSION

The requirement for Notch signaling during mouse somitogenesis

In our current study, we reveal that the cNICD on/off state is not required for somite boundary formation during somitogenesis in the mouse. Consistent with this, recent studies in zebrafish embryos suggest that the function of Notch signaling is only to synchronize the oscillations among PSM cells, and that this pathway has no other function during segmentation (Riedel-Kruse et al., 2007; Horikawa et al., 2006; Ozbudak and Lewis, 2008). However, we propose from our current data that Notch signaling has a crucial function also as an output of the segmentation clock during mouse development.

This contention is supported by earlier evidence that *Mesp2* expression is severely downregulated in the absence of Notch signaling (Barrantes et al., 1999; Takahashi et al., 2000). Moreover, it has been shown that constitutive activation of Notch signaling in the paraxial mesoderm induces *Mesp2* transcription without clear on/off cycles (Feller et al., 2008) and it is also evident from other reports that Notch signaling is crucial for the establishment of R-C patterning of somites in the mouse (Takahashi et al., 2000; Takahashi et al., 2003; Feller et al., 2008). These results together suggest that the function of Notch signaling is not only to synchronize oscillations but that Notch acts also as an important output signal of the segmentation clock, at least in mouse somitogenesis. We thus speculate that Notch signaling is a key factor that mediates the transduction of clock activities into the morphological segmental pattern by regulating *Mesp2* expression. However, it is known that several oscillating components in Notch, Wnt and Fgf signaling pathways are coordinated to generate the segmentation clock network in mice. Hence, *Mesp2* transcription might not be regulated by Notch signaling alone and several pathways might govern the spatiotemporal pattern of *Mesp2* expression. The coordination of these complex networks might well be fundamental to normal somitogenesis.

A new model for the establishment of R-C polarity during somitogenesis

Based on our present findings, we propose a new function for oscillating Notch signaling, which is translated into the R-C polarity of a somite via the regulation of *Mesp2* expression in the anterior PSM. Previous models have proposed that the establishment of R-C polarity requires cell-cell communication (Takahashi et al., 2003; Dale and Pourquie, 2000), whereas we propose a model in which a

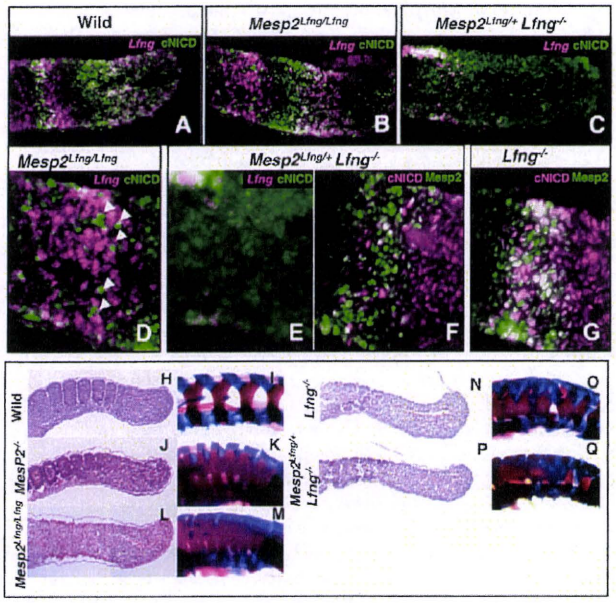

Fig. 6. Exogenous *Lfng* under the control of the *Mesp2* promoter does not rescue the phenotype of the *Mesp2*$^{-/-}$ or *Lfng*$^{-/-}$ mouse. (**A-G**) Sections of E11.5 embryos double stained for *Lfng* mRNA and cNICD (A-E) or for Mesp2 and cNICD (F,G). Higher magnification images of B and C are shown in D and E, respectively. In the *Mesp2*$^{Lfng/Lfng}$ embryo, cNICD formation (B,D, *n*=3) is suppressed in the anterior PSM. The arrowheads in D indicate *Lfng* non-expressing cells that maintain cNICD formation cell-autonomously. In the *Mesp2*$^{Lfng/+}$*Lfng*$^{-/-}$ embryos, cNICD (F, *n*=5) is effectively suppressed in the Mesp2-expressing cells compared with *Lfng*-null embryos (G, *n*=6). (**H-Q**) Comparison of the segmental morphologies in the E11.5 embryonic tail region (H,J,L,N,P) and E17.5 vertebral region (I,K,M,O,Q) among the different genotypes indicated. Neither the *Mesp2*$^{Lfng/Lfng}$ (L,M) nor *Mesp2*$^{Lfng/+}$*Lfng*$^{-/-}$ (P,Q) mice show any recovery of the *Mesp2*$^{-/-}$ (J,K) or *Lfng*$^{-/-}$ (N,O) phenotypes. Number of samples: H, *n*=4; I, *n*=6; J, *n*=3; K, *n*=4; L, *n*=3; M, *n*=6; N, *n*=3; O, *n*=6; P, *n*=3; Q, *n*=7.

cell-autonomous mechanism utilizes Notch signaling oscillation in the posterior PSM. This notion is further supported by computer simulations, in which we found that an appropriate translation of spatiotemporal information provided by the traveling wave of cNICD is sufficient to create the dynamic *Mesp2* expression pattern, i.e. on/off cycles and rostral localization (Fig. 5B; see Movie 1 in the supplementary material). In these simulation experiments, the generation of the traveling wave was based on the earlier work of Lewis (Palmeirim et al., 1997), and the translation of the wave information into *Mesp2* expression was modeled on the gene network that we elucidated previously (Oginuma et al., 2008; Yasuhiko et al., 2006). In the model, the cNICD wave, an activator of *Mesp2*, travels from the posterior to the anterior, whereas the levels of Fgf, a repressor of *Mesp2*, are higher toward the posterior. Consequently, as a single wave passes through a nascent somite, the net transcriptional activation of *Mesp2*, which reflects the amount of cNICD subtracted by the amount of Fgf, is higher toward the rostral part of the presumptive somite. The resulting gradient of Mesp2 activity might thus allow PSM cells to establish a rostral identity and the segmental border. Hence, this is the first model to demonstrate that R-C polarity in the somite is generated as a direct output of the segmentation clock.

The repression of Tbx6, an activator of *Mesp2*, downstream of Mesp2 is another important component in our model. This regulatory module prevents *Mesp2* expression after one traveling wave of cNICD has passed, and thus fixes the R-C gradient pattern of Mesp2. The next wave of Notch signaling cannot affect the Mesp2 pattern created by the former wave. To reproduce the intensive degradation of Tbx6 at anterior regions, we had to adjust the parameters for Tbx6 degradation. We did not need to change any of the other standard parameters we initially chose, suggesting that the qualitative features of the model are not so sensitive to the quantitative values of the parameters. In our simulation analysis, however, we did not reproduce the sharp anterior boundaries of Tbx6 and Mesp2 accumulation (green and black lines, respectively, in Fig. 5B; see Movie 1 in the supplementary material) that have been observed in vivo. To create a sharp boundary of Tbx6 and Mesp2, which should be required to create a fine segmentation boundary, further adjustment of the parameters or another mechanism might be required. In this regard, the next important challenge will be to investigate the molecular basis of the sharpening expression boundaries of Tbx6 and Mesp2, and ultimately to understand how analog inputs (such as sequential wave patterns of oscillation) are converted into digital outputs (such as the square-like stair patterns of the segmental border).

Functions of Lfng in the posterior and anterior PSM during mouse somitogenesis

We also demonstrate from our present data that the oscillatory expression of *Lfng* is both required and sufficient for normal somitogenesis. However, this result will probably be viewed somewhat controversially given the recent findings that have underscored the significance of Lfng expression in the anterior PSM during this process, at least after E10.5 (Shifley et al., 2008; Stauber et al., 2009). The authors of these reports produced transgenic mice harboring *Lfng* expression without oscillation. Their data indicate that cNICD oscillation is disrupted, but that normal segmented somites form, after E10.5 and they concluded that oscillating *Lfng* expression is required only for early stage, but not later stage, somitogenesis (Shifley et al., 2008; Stauber et al., 2009). We wish therefore to discuss some possible explanations for the discrepancies between our current findings and these previous experimental results.

One possibility is that the common expression profiles between our *Hes7>Lfng* mouse and the mice studied in previous reports is important. We demonstrate here that *Hes7* and *Lfng* expression manifest a waved pattern within the Tbx6 expression domain, which includes a part of the anterior PSM. Therefore, in our *Hes7>Lfng* mouse, oscillating *Lfng* expression also exists in the anterior PSM, but not as a stabilized pattern. We suspect that the transgenic mice analyzed in previous reports lack oscillating *Lfng* expression in the posterior PSM but the oscillation might exist in the anterior PSM as well, and thus we speculate that the oscillating *Lfng* expression in the posterior PSM is not required after E10.5, but that in the anterior PSM might be sufficient for normal somitogenesis. Another possibility is that the slightly oscillating expression reported previously might be responsible for the rescue event. Previous studies have shown that two distinct enhancers are involved in the oscillatory expression of *Lfng*, one of which is disrupted in the mouse reported by Shifley et al. (Shifley et al., 2008), and a slight cyclic expression of *Lfng* exists in the mouse generated by Stauber et al. (Stauber et al., 2009). Hence, one possible interpretation for these discrepancies is that the slight cyclic expression of *Lfng* might be sufficient for normal development in the enhancer-specific

knockout mouse after E10.5 somitogenesis, but not prior to E10.5. It is reasonable to assume that the requirement of Notch clock oscillation by *Lfng* changes during somitogenesis and is lesser at later stages, as now suggested by a number of studies (Shifley et al., 2008; Stauber et al., 2009).

Acknowledgements
We thank Ryoichiro Kageyama (Kyoto University) for providing the *Hes7* promoter and enhancer cassette, Aya Satoh, Nobuo Sasaki and Yusuke Okubo (National Institute of Genetics) for animal care and the preparation of embryo samples and Mariko Ikumi, Eriko Ikeno and Shinobu Watanabe (National Institute of Health Sciences) for technical assistance. This work was supported in part by Grants-in-Aid for Scientific Research on Priority Areas, Dynamics of Extracellular Environments, and by the National BioResource Project from the Ministry of Education, Culture, Sports, Science and Technology, Japan.

Competing interests statement
The authors declare no competing financial interests.

Supplementary material
Supplementary material for this article is available at
http://dev.biologists.org/lookup/suppl/doi:10.1242/dev.044545/-/DC1

References

Aulehla, A. and Johnson, R. L. (1999). Dynamic expression of lunatic fringe suggests a link between notch signaling and an autonomous cellular oscillator driving somite segmentation. *Dev. Biol.* **207**, 49-61.
Aulehla, A., Wehrle, C., Brand-Saberi, B., Kemler, R., Gossler, A., Kanzler, B. and Herrmann, B. G. (2003). Wnt3a plays a major role in the segmentation clock controlling somitogenesis. *Dev. Cell* **4**, 395-406.
Aulehla, A., Wiegraebe, W., Baubet, V., Wahl, M. B., Deng, C., Taketo, M., Lewandoski, M. and Pourquie, O. (2008). A beta-catenin gradient links the clock and wavefront systems in mouse embryo segmentation. *Nat. Cell Biol.* **10**, 186-193.
Barrantes, I. B., Elia, A. J., Wunsch, K., Hrabe de Angelis, M. H., Mak, T. W., Rossant, J., Conlon, R. A., Gossler, A. and de la Pompa, J. L. (1999). Interaction between Notch signalling and Lunatic fringe during somite boundary formation in the mouse. *Curr. Biol.* **9**, 470-480.
Bessho, Y., Hirata, H., Masamizu, Y. and Kageyama, R. (2003). Periodic repression by the bHLH factor Hes7 is an essential mechanism for the somite segmentation clock. *Genes Dev.* **17**, 1451-1456.
Cole, S. E., Levorse, J. M., Tilghman, S. M. and Vogt, T. F. (2002). Clock regulatory elements control cyclic expression of Lunatic fringe during somitogenesis. *Dev. Cell* **3**, 75-84.
Dale, K. J. and Pourquie, O. (2000). A clock-work somite. *BioEssays* **22**, 72-83.
Delfini, M. C., Dubrulle, J., Malapert, P., Chal, J. and Pourquie, O. (2005). Control of the segmentation process by graded MAPK/ERK activation in the chick embryo. *Proc. Natl. Acad. Sci. USA* **102**, 11343-11348.
Dequeant, M. L. and Pourquie, O. (2008). Segmental patterning of the vertebrate embryonic axis. *Nat. Rev. Genet.* **9**, 370-382.
Dequeant, M. L., Glynn, E., Gaudenz, K., Wahl, M., Chen, J., Mushegian, A. and Pourquie, O. (2006). A complex oscillating network of signaling genes underlies the mouse segmentation clock. *Science* **314**, 1595-1598.
Evrard, Y. A., Lun, Y., Aulehla, A., Gan, L. and Johnson, R. L. (1998). lunatic fringe is an essential mediator of somite segmentation and patterning. *Nature* **394**, 377-381.
Feller, J., Schneider, A., Schuster-Gossler, K. and Gossler, A. (2008). Noncyclic Notch activity in the presomitic mesoderm demonstrates uncoupling of somite compartmentalization and boundary formation. *Genes Dev.* **22**, 2166-2171.
Horikawa, K., Ishimatsu, K., Yoshimoto, E., Kondo, S. and Takeda, H. (2006). Noise-resistant and synchronized oscillation of the segmentation clock. *Nature* **441**, 719-723.
Lewis, J. (2003). Autoinhibition with transcriptional delay: a simple mechanism for the zebrafish somitogenesis oscillator. *Curr. Biol.* **13**, 1398-1408.
McGrew, M. J., Dale, J. K., Fraboulet, S. and Pourquie, O. (1998). The lunatic fringe gene is a target of the molecular clock linked to somite segmentation in avian embryos. *Curr. Biol.* **8**, 979-982.
Morales, A. V., Yasuda, Y. and Ish-Horowicz, D. (2002). Periodic Lunatic fringe expression is controlled during segmentation by a cyclic transcriptional enhancer responsive to notch signaling. *Dev. Cell* **3**, 63-74.
Morimoto, M., Takahashi, Y., Endo, M. and Saga, Y. (2005). The Mesp2 transcription factor establishes segmental borders by suppressing Notch activity. *Nature* **435**, 354-359.
Nakajima, Y., Morimoto, M., Takahashi, Y., Koseki, H. and Saga, Y. (2006). Identification of Epha4 enhancer required for segmental expression and the regulation by Mesp2. *Development* **133**, 2517-2525.
Niwa, Y., Masamizu, Y., Liu, T., Nakayama, R., Deng, C. X. and Kageyama, R. (2007). The initiation and propagation of Hes7 oscillation are cooperatively regulated by Fgf and notch signaling in the somite segmentation clock. *Dev. Cell* **13**, 298-304.
Oginuma, M., Niwa, Y., Chapman, D. L. and Saga, Y. (2008). Mesp2 and Tbx6 cooperatively create periodic patterns coupled with the clock machinery during mouse somitogenesis. *Development* **135**, 2555-2562.
Ozbudak, E. M. and Lewis, J. (2008). Notch signalling synchronizes the zebrafish segmentation clock but is not needed to create somite boundaries. *PLoS Genet.* **4**, e15.
Palmeirim, I., Henrique, D., Ish-Horowicz, D. and Pourquie, O. (1997). Avian hairy gene expression identifies a molecular clock linked to vertebrate segmentation and somitogenesis. *Cell* **91**, 639-648.
Riedel-Kruse, I. H., Muller, C. and Oates, A. C. (2007). Synchrony dynamics during initiation, failure, and rescue of the segmentation clock. *Science* **317**, 1911-1915.
Sakai, K. and Miyazaki, J. (1997). A transgenic mouse line that retains Cre recombinase activity in mature oocytes irrespective of the cre transgene transmission. *Biochem. Biophys. Res. Commun.* **237**, 318-324.
Shifley, E. T., Vanhorn, K. M., Perez-Balaguer, A., Franklin, J. D., Weinstein, M. and Cole, S. E. (2008). Oscillatory lunatic fringe activity is crucial for segmentation of the anterior but not posterior skeleton. *Development* **135**, 899-908.
Stauber, M., Sachidanandan, C., Morgenstern, C. and Ish-Horowicz, D. (2009). Differential axial requirements for lunatic fringe and Hes7 transcription during mouse somitogenesis. *PLoS One* **4**, e7996.
Takahashi, Y., Koizumi, K., Takagi, A., Kitajima, S., Inoue, T., Koseki, H. and Saga, Y. (2000). Mesp2 initiates somite segmentation through the Notch signalling pathway. *Nat. Genet.* **25**, 390-396.
Takahashi, Y., Inoue, T., Gossler, A. and Saga, Y. (2003). Feedback loops comprising Dll1, Dll3 and Mesp2, and differential involvement of Psen1 are essential for rostrocaudal patterning of somites. *Development* **130**, 4259-4268.
Takahashi, Y., Yasuhiko, Y., Kitajima, S., Kanno, J. and Saga, Y. (2007). Appropriate suppression of Notch signaling by Mesp factors is essential for stripe pattern formation leading to segment boundary formation. *Dev. Biol.* **304**, 593-603.
Wahl, M. B., Deng, C., Lewandoski, M. and Pourquie, O. (2007). FGF signaling acts upstream of the NOTCH and WNT signaling pathways to control segmentation clock oscillations in mouse somitogenesis. *Development* **134**, 4033-4041.
Watanabe, T., Sato, Y., Saito, D., Tadokoro, R. and Takahashi, Y. (2009). EphrinB2 coordinates the formation of a morphological boundary and cell epithelialization during somite segmentation. *Proc. Natl. Acad. Sci. USA* **106**, 7467-7472.
Yasuhiko, Y., Haraguchi, S., Kitajima, S., Takahashi, Y., Kanno, J. and Saga, Y. (2006). Tbx6-mediated Notch signaling controls somite-specific Mesp2 expression. *Proc. Natl. Acad. Sci. USA* **103**, 3651-3656.
Zhang, N. and Gridley, T. (1998). Defects in somite formation in lunatic fringe-deficient mice. *Nature* **394**, 374-377.

LETTER

doi:10.1038/nature09473

Structural basis for semaphorin signalling through the plexin receptor

Terukazu Nogi[1], Norihisa Yasui[1]†, Emiko Mihara[1], Yukiko Matsunaga[1], Masanori Noda[2], Naoya Yamashita[3], Toshihiko Toyofuku[4], Susumu Uchiyama[2], Yoshio Goshima[3], Atsushi Kumanogoh[4] & Junichi Takagi[1]

Semaphorins and their receptor plexins constitute a pleiotropic cell-signalling system that is used in a wide variety of biological processes, and both protein families have been implicated in numerous human diseases[1–4]. The binding of soluble or membrane-anchored semaphorins to the membrane-distal region of the plexin ectodomain activates plexin's intrinsic GTPase-activating protein (GAP) at the cytoplasmic region, ultimately modulating cellular adhesion behaviour[5]. However, the structural mechanism underlying the receptor activation remains largely unknown. Here we report the crystal structures of the semaphorin 6A (Sema6A) receptor-binding fragment and the plexin A2 (PlxnA2) ligand-binding fragment in both their pre-signalling (that is, before binding) and signalling (after complex formation) states. Before binding, the Sema6A ectodomain was in the expected 'face-to-face' homodimer arrangement, similar to that adopted by Sema3A and Sema4D, whereas PlxnA2 was in an unexpected 'head-on' homodimer arrangement. In contrast, the structure of the Sema6A–PlxnA2 signalling complex revealed a 2:2 heterotetramer in which the two PlxnA2 monomers dissociated from one another and docked onto the top face of the Sema6A homodimer using the same interface as the head-on homodimer, indicating that plexins undergo 'partner exchange'. Cell-based activity measurements using mutant ligands/receptors confirmed that the Sema6A face-to-face dimer arrangement is physiologically relevant and is maintained throughout signalling events. Thus, homodimer-to-heterodimer transitions of cell-surface plexin that result in a specific orientation of its molecular axis relative to the membrane may constitute the structural mechanism by which the ligand-binding 'signal' is transmitted to the cytoplasmic region, inducing GAP domain rearrangements and activation.

Both semaphorins and plexins contain, at the amino terminus of their ectodomain, a ~500-residue sema domain followed by a short (~50 residues) plexin–semaphorin–integrin (PSI) domain. Those regions corresponding to the sema plus PSI segment of Sema6A ($Sema6A_{SP}$, residues 19–570) and PlxnA2 ($PlxnA2_{SP}$, residues 38–561) that mediate ligand–receptor interaction were first expressed in mammalian cell lines, and then purified and crystallized (Supplementary Fig. 1). Structures of $Sema6A_{SP}$ and $PlxnA2_{SP}$ were determined at 2.5 Å and 2.1 Å resolution, respectively (Fig. 1a, b, Supplementary Tables 1 and 2, and Supplementary Results). In both proteins, the sema domain displays a seven-bladed β-propeller fold very similar to previously determined structures of Sema3A[6], Sema4D[7] and Met[8]. In addition to the long 'extrusion' within blade 5 described previously[7] (hereafter called extrusion 2), we noted a second insertion between blades 1 and 2 that proved characteristic to all sema domains (hereafter called extrusion 1) (Fig. 1e).

In the $Sema6A_{SP}$ crystal, monomers make contact with one another using the upper rim of the β-propeller, thereby assuming a 'face-to-face' dimer configuration (Fig. 1a). This dimeric configuration is essentially identical to that seen in the crystal structures of the Sema3A and Sema4D sema domains (Supplementary Fig. 2a). The location of the loops involved in the dimerization is precisely conserved among the three semaphorins, with the exception of the N-terminal region's participation in Sema6A (Supplementary Fig. 2b). Surprisingly, $PlxnA2_{SP}$ also assumes a dimeric configuration in the crystal, albeit with a markedly different mode compared to that observed in the semaphorin sema domains (Fig. 1b). The two $PlxnA2_{SP}$ fragments in the asymmetric unit are related by a non-crystallographic two-fold axis and interact with each other by using a flat surface located at the side of the β-propeller, exhibiting a 'head-on' configuration twisted orthogonally, in contrast to the face-to-face configuration observed in the known semaphorin structures. All the key residues involved in the dimerization are well conserved among the A-type plexin family (Supplementary Results and Supplementary Fig. 3), indicating the physiological relevance of the dimerization. Analytical ultracentrifugation sedimentation velocity experiments performed on the $Sema6A_{SP}$ protein confirmed that it does indeed form a dimer in solution with a dissociation constant (K_d) value of 3.5 μM (Supplementary Fig. 4). The dimerization affinity for $PlxnA2_{SP}$, however, was extremely low ($K_d > 300$ μM) and could not be definitively determined (Supplementary Fig. 5).

We next crystallized the Sema6A–PlxnA2 complex by mixing $Sema6A_{SP}$ and $PlxnA2_{SP}$ at an equimolar concentration, obtaining a structure at 3.6 Å resolution (Supplementary Results, Supplementary Table 3 and Supplementary Fig. 6). The $Sema6A_{SP}$ and $PlxnA2_{SP}$ molecules constitute a 2:2 complex in the crystal, which contained a crystallographic two-fold symmetry (Fig. 1c). The two $Sema6A_{SP}$ molecules in the complex formed the same face-to-face dimer as was observed in the plexin-free state (Supplementary Fig. 7a). On the other hand, the $PlxnA2_{SP}$ head-on homodimer was no longer present in the complex, and the two plexin molecules independently docked onto the two Sema6A monomers with their carboxy-terminal PSI domains emanating away diagonally. Despite their participation in different molecular interactions, there were no major changes in the structure of individual $Sema6A_{SP}$ and $PlxnA2_{SP}$ monomers, including the conformation of the loops at the interface, upon the complex formation (root mean squared deviation of 0.70 Å for $Sema6A_{SP}$ and 0.80 Å for $PlxnA2_{SP}$, respectively; Supplementary Figs 7 and 8). At the interface, the Sema6A side showed positively charged surface potentials whereas the PlxnA2 side was negatively charged, indicating that complex formation is driven mainly by electrostatic interactions (Fig. 1d).

We subsequently mutated a select number of interface residues on Sema6A to see whether these mutations disrupt plexin binding. The H212N mutation is expected to create a novel N212-D213-S214 glycosylation sequon and place a large carbohydrate obstacle at the heart of the interface (Fig. 1d and Supplementary Fig. 8). Another mutation, K393E, is expected to convert the electrostatic interaction between

[1]Laboratory of Protein Synthesis and Expression, Institute for Protein Research, Osaka University, 3-2 Yamadaoka, Suita, Osaka 565-0871, Japan. [2]Department of Biotechnology, Graduate School of Engineering, Osaka University, 2-1 Yamadaoka, Suita, Osaka 565-0871, Japan. [3]Department of Molecular Pharmacology & Neurobiology, Yokohama City University Graduate School of Medicine, 3-9 Fukuura, Kanazawa, Yokohama 236-0004, Japan. [4]Department of Immunopathology, Immunology Frontier Research Center, Research Institute for Microbial Diseases, Osaka University, 3-1 Yamadaoka, Suita, Osaka 565-0871, Japan. †Present address: Department of Biochemistry and Molecular Biology, The University of Chicago, 929 East 57th Street, W234, Chicago, Illinois 60637, USA.

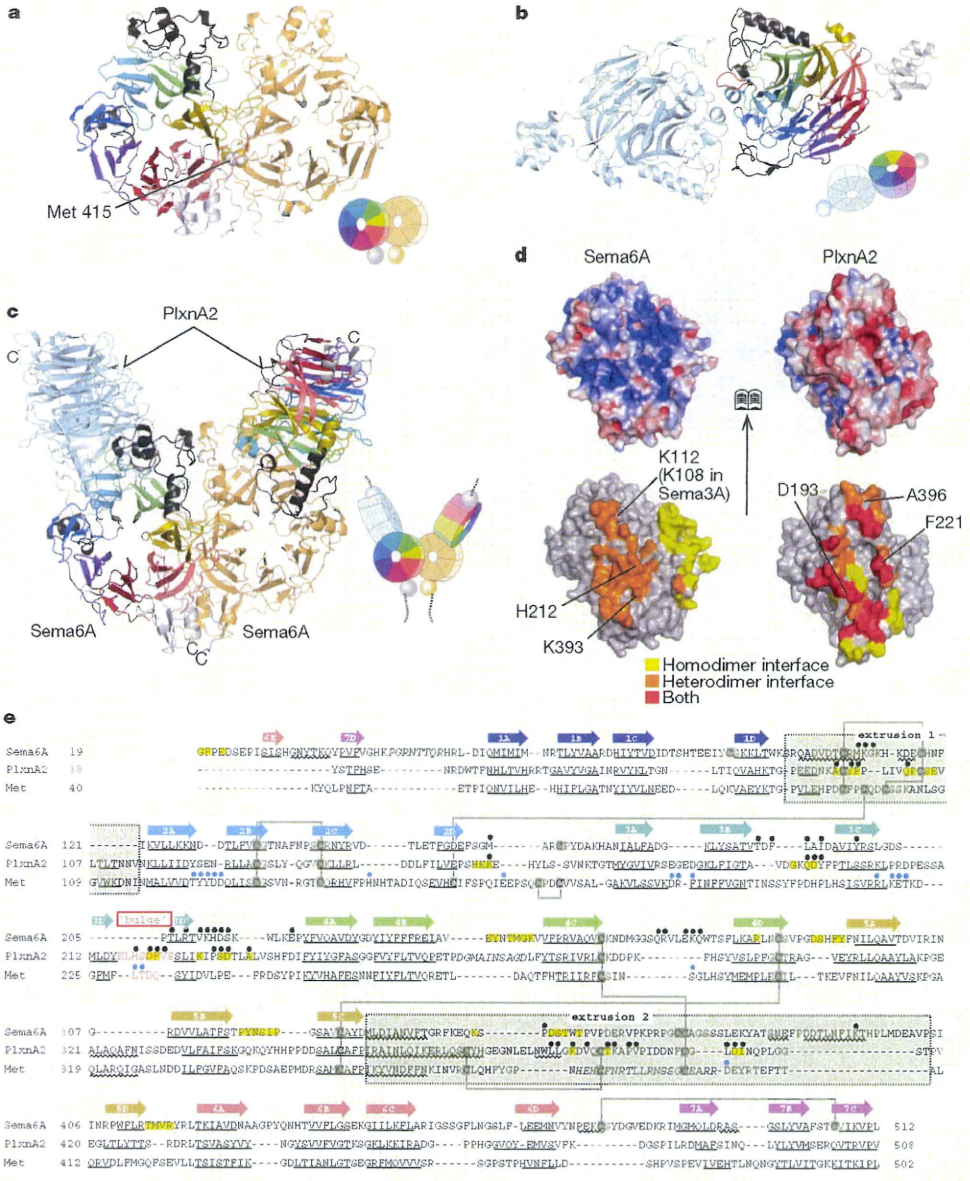

Figure 1 | Crystal structure of Sema6A and PlxnA2 ectodomain fragments in pre-signalling and post-signalling states. a–c, Structures of the Sema6A face-to-face homodimer (**a**), PlxnA2 head-on dimer (**b**) and Sema6A–PlxnA2 2:2 complex (**c**). Individual propeller blades are coloured differently in one monomer. Arrangement of the toroidal propeller domains within the structure is schematically depicted in the cartoon next to each ribbon presentation. **d**, Open-book view of the Sema6A–PlxnA2 interface surface coloured by electrostatic potential (top panel) and by the residue-wise contribution to the interface (bottom panel). **e**, Structural alignment of the sema domains. Secondary structure elements are denoted by straight (strands) or wavy (helices) lines below each sequence. Residues in the homodimer interface are highlighted in yellow. Dots above the sequence indicate residues involved in the heteromeric interaction in the Sema6A–PlxnA2 complex (black) or in the Met–HGF complex (blue). Cysteines are shown with a grey background and disordered residues are shown in italics. Residues in a bulged insertion in the middle of strand 3D are shown in red.

Lys 393 and Asp 193 of the plexin into a repulsive one (Supplementary Fig. 8). When these mutations were introduced into the soluble Sema6A–alkaline phosphatase (AP) fusion protein, the binding of the mutant Sema6A–AP to the wild-type PlxnA2 expressed on HEK cells was markedly reduced or virtually absent (Fig. 2a), confirming the authenticity of the interface. As the same effect was observed when PlxnA4-expressing cells were used (data not shown), it is likely that the same binding site is used for the recognition of both plexin receptor subtypes.

Sema6A and Sema3A show similar biological activity on neurons and display the same plexin-type specificity[9,10], indicating that their plexin recognition sites are structurally conserved. In fact, Lys 112 in Sema6A that lies very close to the interface corresponds to the Sema3A residue Lys 108, which has been shown to be critical in signalling events[11] (Fig. 1d and Supplementary Fig. 2b), further supporting this notion. We therefore mutated putative interface residues in Sema3A and tested their activity. As shown in Fig. 2b, Sema3A–AP proteins carrying interface mutations—including H216N (corresponding to Sema6A H212N glycosylation mutant) and R404E (corresponding to Sema6A K393E charge reversal mutant)—had lost their collapse-inducing activity, even though their binding to the high-affinity neuropilin-1 receptor remained intact (Fig. 2c). This indicates that the same interface is used by the neuropilin-bound Sema3A on the cell surface to bind to, and signal through, plexin receptors in neurons.

We next mutated key interface residues in the PlxnA2 sema domain and evaluated their ability to bind Sema6A. Ala 396 of PlxnA2 is

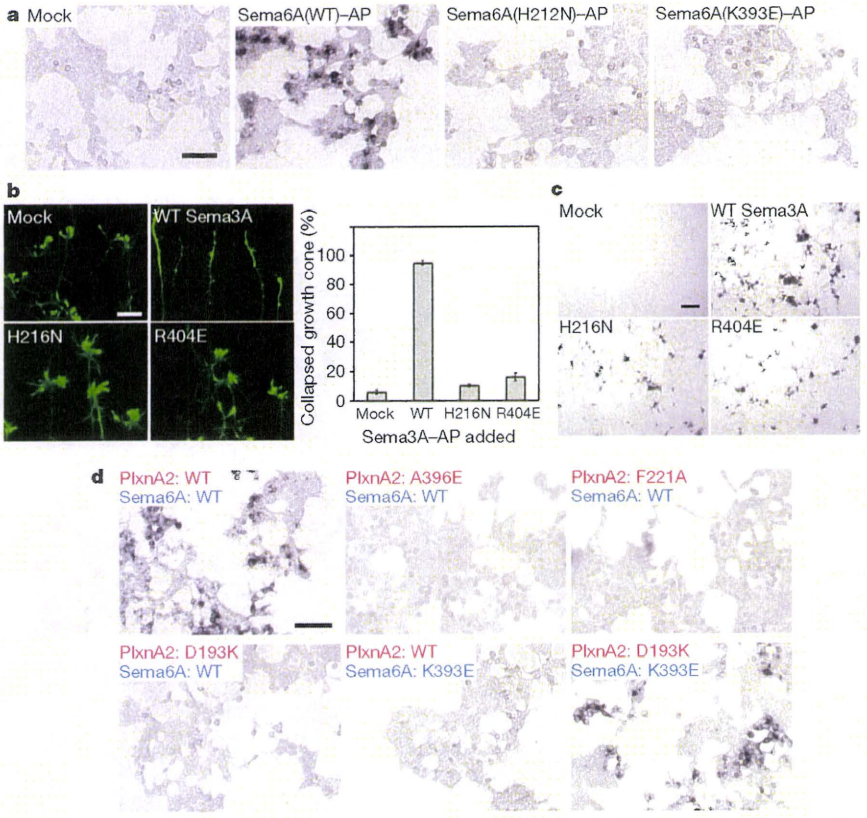

Figure 2 | Authenticity of the semaphorin–plexin interface is confirmed by mutational experiments. **a**, Binding of Sema6A–AP fusion protein to plexin. HEK293T cells transiently transfected with full-length wild-type PlxnA2 were incubated with either wild-type (WT) or mutant (H212N and K393E) Sema6A–AP at 100 nM for 90 min, fixed, and stained for AP activity. Scale bar, 100 μm. **b**, Activity loss of Sema3A mutants. Conditioned media containing wild-type, H216N or R404E Sema3A–AP were incubated with chick DRG neurons and visualized with Alexa488-conjugated phalloidin. Scale bar, 25 μm. The percentage of collapsed growth cones was counted and expressed as the mean ± s.e.m. ($n = 9$). **c**, Neuropilin-1 binding activity of Sema3A mutants. COS-7 cells expressing mouse neuropilin-1 were incubated with the same set of conditioned medium used in **b** and the bindings were evaluated by AP activity staining. Scale bar, 200 μm. **d**, Effects of plexin mutations on Sema6A binding. HEK293T cells were transiently transfected with N-terminally Flag-tagged full-length PlxnA2 with indicated mutations and tested for the binding of either wild-type or the K393E mutant version of Sema6A–AP. Scale bar, 100 μm.

located at the heteromeric, but not the homodimeric, interface (Fig. 1d and Supplementary Fig. 8), in agreement with a finding that the A396E mutation in PlxnA2 causes a developmental abnormality in mice due to the lack of ligand binding[10]. We confirmed that the A396E mutant plexin expressed on HEK cells failed to support Sema6A–AP binding (Fig. 2d). Furthermore, an Ala substitution of Phe 221, which buries more than 170 $Å^2$ of the accessible surface in the complex, resulted in a negligible binding of Sema6A (Fig. 2d). Another mutation, D193K, which destroys salt bridge formation between Lys 393 of Sema6A, also eliminated the binding. This lack of Sema6A binding, however, did not stem from the impaired transportation of mutant plexins to the cell surface, as evidenced by the comparable level of anti-Flag immunostaining on the cell surface (Supplementary Fig. 9). Remarkably, when both charge-reversal mutants (that is, plexin D193K and Sema6A K393E) were combined, binding was completely recovered (Fig. 2d). These results strongly indicate that the current complex structure captures the genuine receptor–ligand interaction. Notably, PlxnA2 and Sema6A use an identical set of loops for heteromeric recognition (Fig. 1e, denoted by black dots). The resulting binding surface, in both proteins, is centred at blade 3, bounded by extrusions 1 and 2 at both sides, and located atop the propeller opposite the PSI domain. As Met also uses roughly the same region to interact with truncated HGF ligand (Fig. 1e, blue dots)[8], it is possible that the location of an important functional epitope is shared among all sema domains.

The strictly conserved dimeric configuration seen in all semaphorins prompted us to test the functional importance of the Sema6A dimer. Methionine 415 is located at the periphery of the dimerization interface, pointing towards the corresponding residue in the partner molecule (Fig. 1a). Mutating Met 415 to Cys resulted in a covalent disulphide bond formation across the dimer interface in both cell-surface full-length Sema6A proteins (Fig. 3a), as well as in the soluble ectodomain fragment (Fig. 3b). We purified wild-type and dimeric (M415C) versions of the soluble ectodomain fragments of Sema6A and tested their ability to induce morphological changes in PlxnA4-expressing HEK cells. The locked dimer Sema6A (M415C) exhibited strong contraction activity towards those HEK cells stably expressing PlxnA4 over a concentration range of 10–300 nM (Fig. 3c), but not towards the control cells (data not shown). In contrast, very high concentrations (>3 μM) of the wild-type Sema6A ectodomain was required to elicit a modest level of cell contraction, indicating that it has >100-fold lower activity compared to the dimeric mutant. Dimerization-dependent collapse activity has already been reported using the Sema6A–Fc fusion protein[12]. Unlike the Fc or AP fusion strategy, which brings about dimerization of the recombinant proteins via Fc or AP moiety[13], our disulphide-bonded Sema6A dimerization did not permit dissociation and fixed the relative orientation of the two sema domains. Therefore, our results indicate that the heterotetrameric configuration of the Sema6A– PlxnA2 complex seen in the crystal structure represents a signalling-competent conformation maintained throughout the signal transduction process.

It has been shown that the cytoplasmic domain of plexin has the potential to form a homodimer[14]. It has also been postulated that at the extracellular region the sema domain can interact with the stalk region of the molecule[15]. Our results now reveal a third possible homophilic interaction mode in plexin: the sema–sema homodimerization.

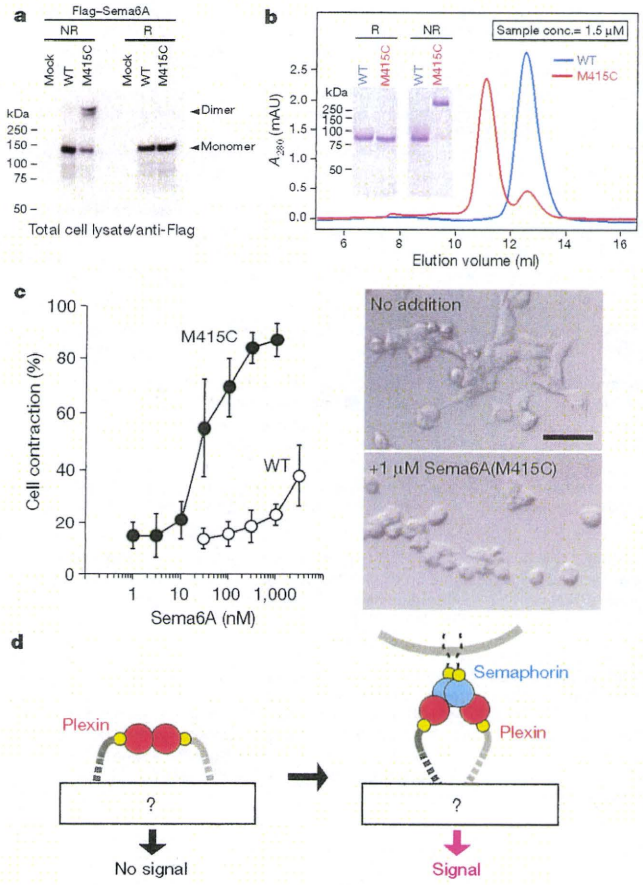

Figure 3 | The Sema6A face-to-face homodimer represents a signalling-competent active conformation. a, The dimer formation of Sema6A expressed on the cell surface. Lysates of HEK293T cells that had been transfected with empty vector (mock), Flag–Sema6A (WT), or Flag–Sema6A with the M415C mutation (M415C) were subjected to SDS–PAGE under reducing (R) or non-reducing (NR) conditions, followed by immunoblotting using anti-Flag antibody. **b**, $Sema6A_{SP}$ ectodomain fragments (WT or M415C) were subjected to gel filtration chromatography. The peak elution positions for the wild type and M415C mutant corresponded to 106 and 219 kDa, respectively. SDS–PAGE analysis (inset) confirmed the >90% formation of a disulphide-linked homodimer in the M415C mutant. **c**, Signalling activities of soluble Sema6A proteins. Purified $Sema6A_{SP}$ proteins (WT or M415C) were tested for their ability to induce contraction of HEK293T cells stably expressing PlxnA4. Representative images of cell morphologies both before and after the stimulation are also shown (right). Scale bar, 50 μm. **d**, Possible structural mechanism of semaphorin-induced plexin signalling. Transition from the head-on *cis* homodimer of plexin (left) to the semaphorin-engaged complex (right) changes the relative orientation of the plexin molecular axis. This conformational change is transmitted through the stalk region (thick dotted line) and alters the conformation (for example, dimerization state) of the cytoplasmic GAP domain, resulting in signal initiation. The closer positioning of the two plexin tails in the active conformation is drawn arbitrarily and should be taken as an example, because the association states of the transmembrane and cytoplasmic regions before and after receptor activation remain unknown.

Although affinity for the plexin sema domain homodimerization in solution was estimated to be extremely low (>300 μM), homomeric interactions with comparable degrees of affinity can mediate lateral receptor dimerization[16]. The head-on arrangement of the plexin *cis* dimer requires that the receptor axis be aligned in parallel to the membrane. Such a configuration would be possible in plexins, which have a long 'stalk region' consisting of six immunoglobulin domains interspersed by PSI domains found at the mobile domain boundaries both in integrins and in Met[17,18], thereby enabling the plexin to bend (or bow) its head. Similarly 'bowed' conformations have been postulated in Met as well[17].

Plexins on the resting cell surface assume an 'auto-inhibited' state, with their cytoplasmic GAP domain activity suppressed[19]. It is also accepted that ligand engagement at the extracellular side somehow activates GAP. Recently, crystal structures of the intracellular GAP domains of PlxnA3 and PlxnB1 have been reported by two groups[20,21]. Although it is still unclear how the activity of the GAP domain is structurally regulated (for example, by a monomer/dimer exchange or conformational changes within a single domain), our current structure clearly identifies the structural change that takes place at the extracellular side. In the resting state, plexin assumes an auto-inhibited conformation, possibly by structural constraints stemming from head-on dimerization (Fig. 3d, left). Upon semaphorin engagement, the orientation of the two plexin heads becomes more perpendicularly aligned to the membrane (Fig. 3d, right). This conformational change is then transmitted, through the long stalk and the transmembrane domain, to the cytoplasmic region, leading to activation of the GAP domain and/or recruitment of Rho family GTPases. Very recently, a structure determination of the Sema7A–PlxnC1 ectodomain complex was reported[22]. Although they did not solve the structure of the ligand-free PlxnC1, the complex structure was surprisingly similar to the Sema6A–PlxnA2 complex reported here, revealing a 2:2 stoichiometry with near-identical arrangements of each monomer. Although it remains possible that most of the cell-surface plexins in the resting state do not form a head-on dimer and the inactive phenotype is maintained by another type of mechanism[15], the structural conservation observed between the two semaphorin–plexin 'terminal' complexes is strongly indicative of the fundamental importance of this conformation in plexin signal transduction. More structural data are needed regarding the rest of the molecule, particularly the stalk region and the GAP domain, under different activation states, in order to understand fully the mechanism underlying semaphorin-induced plexin signal transduction. Such information may lead to the discovery of novel points of semaphorin signal intervention not limited to the receptor–ligand interface.

METHODS SUMMARY

The mouse Sema6A ectodomain fragment containing residues 19–570 was expressed as a human growth hormone (hGH) fusion protein in CHO lec 3.2.8.1 cells[23], whereas the mouse $PlxnA2_{SP}$ fragment (residues 38–561) containing the C-terminal TARGET tag was stably expressed using HEK293S GnT1$^-$ cells as described previously[24]. Proteins were purified after removing the respective tag sequences and then crystallized. The $Sema6A_{SP}$ crystal with the highest diffraction quality was obtained in a buffer containing 22–24% (wt/vol.) polyethylene glycol (PEG) 1500 and 0.1 M Tris-Cl pH 7.0. $PlxnA2_{SP}$ was crystallized in a buffer containing 24–28% (wt/vol.) PEG 3350, 0–0.2 M NaCl and 0.1 M Tris-Cl pH 8.0–8.5. To determine the structure of the complex, Sema6A and PlxnA2 were mixed at an equimolar ratio and subjected to crystallization. This complex crystal grew in a solution containing 18–25% (wt/vol.) PEG 1000, 0.2–0.3 M $MgCl_2$, 0.1 M Na Cacodylate pH 5.5–6.5. The Sema6A structure was solved by a molecular replacement method using the coordinates of Sema4D (PDB 1OLZ). During molecular replacement phasing of the PlxnA2 crystal, the Met structure (PDB 1SHY) was used as a search model. The complex structure was determined by fitting the above-determined Sema6A and PlxnA2 structures. Single-isomorphous replacement with anomalous scattering (SIRAS) phasing with the Pt-derivative crystal was also incorporated during structural determination of the complex. Preparation of Sema6A–AP or Sema3A–AP fusion proteins, their cell binding analyses, and the growth cone collapse assay using explanted chick dorsal root ganglion (DRG) neurons were performed as previously described[25,26].

Full Methods and any associated references are available in the online version of the paper at www.nature.com/nature.

Received 30 July; accepted 8 September 2010.
Published online 29 September 2010.

1. Tamagnone, L. & Comoglio, P. M. To move or not to move? Semaphorin signalling in cell migration. *EMBO Rep.* **5**, 356–361 (2004).
2. Zhou, Y., Gunput, R. A. & Pasterkamp, R. J. Semaphorin signaling: progress made and promises ahead. *Trends Biochem. Sci.* **33**, 161–170 (2008).
3. Suzuki, K., Kumanogoh, A. & Kikutani, H. Semaphorins and their receptors in immune cell interactions. *Nature Immunol.* **9**, 17–23 (2008).

4. Neufeld, G. & Kessler, O. The semaphorins: versatile regulators of tumour progression and tumour angiogenesis. *Nature Rev. Cancer* **8**, 632–645 (2008).
5. Pasterkamp, R. J. R-Ras fills another GAP in semaphorin signalling. *Trends Cell Biol.* **15**, 61–64 (2005).
6. Antipenko, A. *et al.* Structure of the semaphorin-3A receptor binding module. *Neuron* **39**, 589–598 (2003).
7. Love, C. A. *et al.* The ligand-binding face of the semaphorins revealed by the high-resolution crystal structure of SEMA4D. *Nature Struct. Biol.* **10**, 843–848 (2003).
8. Stamos, J., Lazarus, R. A., Yao, X., Kirchhofer, D. & Wiesmann, C. Crystal structure of the HGF β-chain in complex with the Sema domain of the Met receptor. *EMBO J.* **23**, 2325–2335 (2004).
9. Suto, F. *et al.* Plexin-A4 mediates axon-repulsive activities of both secreted and transmembrane semaphorins and plays roles in nerve fiber guidance. *J. Neurosci.* **25**, 3628–3637 (2005).
10. Renaud, J. *et al.* Plexin-A2 and its ligand, Sema6A, control nucleus-centrosome coupling in migrating granule cells. *Nature Neurosci.* **11**, 440–449 (2008).
11. Merte, J. *et al.* A forward genetic screen in mice identifies Sema3A(K108N), which binds to neuropilin-1 but cannot signal. *J. Neurosci.* **30**, 5767–5775 (2010).
12. Xu, X. M. *et al.* The transmembrane protein semaphorin 6A repels embryonic sympathetic axons. *J. Neurosci.* **20**, 2638–2648 (2000).
13. Le Du, M. H., Stigbrand, T., Taussig, M. J., Menez, A. & Stura, E. A. Crystal structure of alkaline phosphatase from human placenta at 1.8 Å resolution. Implication for a substrate specificity. *J. Biol. Chem.* **276**, 9158–9165 (2001).
14. Tong, Y. *et al.* Binding of Rac1, Rnd1, and RhoD to a novel Rho GTPase interaction motif destabilizes dimerization of the plexin-B1 effector domain. *J. Biol. Chem.* **282**, 37215–37224 (2007).
15. Takahashi, T. & Strittmatter, S. M. Plexina1 autoinhibition by the plexin sema domain. *Neuron* **29**, 429–439 (2001).
16. Chaudhry, C., Weston, M. C., Schuck, P., Rosenmund, C. & Mayer, M. L. Stability of ligand-binding domain dimer assembly controls kainate receptor desensitization. *EMBO J.* **28**, 1518–1530 (2009).
17. Niemann, H. H. *et al.* Structure of the human receptor tyrosine kinase met in complex with the *Listeria* invasion protein InlB. *Cell* **130**, 235–246 (2007).
18. Luo, B. H. & Springer, T. A. Integrin structures and conformational signaling. *Curr. Opin. Cell Biol.* **18**, 579–586 (2006).
19. Oinuma, I., Ishikawa, Y., Katoh, H. & Negishi, M. The Semaphorin 4D receptor Plexin-B1 is a GTPase activating protein for R-Ras. *Science* **305**, 862–865 (2004).
20. He, H., Yang, T., Terman, J. R. & Zhang, X. Crystal structure of the plexin A3 intracellular region reveals an autoinhibited conformation through active site sequestration. *Proc. Natl Acad. Sci. USA* **106**, 15610–15615 (2009).
21. Tong, Y. *et al.* Structure and function of the intracellular region of the plexin-B1 transmembrane receptor. *J. Biol. Chem.* **284**, 35962–35972 (2009).
22. Liu, H. *et al.* Structural basis of semaphorin-plexin recognition and viral mimicry from Sema7A and A39R complexes with plexinC1. *Cell* **142**, 749–761 (2010).
23. Stanley, P. Chinese hamster ovary cell mutants with multiple glycosylation defects for production of glycoproteins with minimal carbohydrate heterogeneity. *Mol. Cell. Biol.* **9**, 377–383 (1989).
24. Tabata, S. *et al.* A rapid screening method for cell lines producing singly-tagged recombinant proteins using the "TARGET tag" system. *J. Proteomics* **73**, 1777–1785 (2010).
25. Toyofuku, T. *et al.* Repulsive and attractive semaphorins cooperate to direct the navigation of cardiac neural crest cells. *Dev. Biol.* **321**, 251–262 (2008).
26. Goshima, Y. *et al.* A novel action of collapsin: collapsin-1 increases antero- and retrograde axoplasmic transport independently of growth cone collapse. *J. Neurobiol.* **33**, 316–328 (1997).

Supplementary Information is linked to the online version of the paper at www.nature.com/nature.

Acknowledgements We would like to thank Y. Yamada, N. Matsugaki and N. Igarashi of Photon Factory and Y. Kawano and N. Shimizu of SPring-8 BL-41XU for their help with the X-ray data collection; A. Rowe for discussions on the sedimentation equilibrium data analysis; C. Wu for performing the Sema6A–AP binding assay; K. Tamura-Kawakami and M. Nampo for their technical support; and M. Nakano for preparation of the manuscript. This work was supported in part by a 'Target Proteins Research Program (TPRP)' grant from the Ministry of Education, Culture, Sports, Science and Technology of Japan (MEXT).

Author Contributions T.N. and J.T. conceived the project. No.Y. and E.M. expressed, purified and crystallized the proteins. Y.M., Na.Y. and T.T. performed cell biological assays. M.N. and S.U. performed analytical ultracentrifugation experiments. T.N. and No.Y. collected X-ray diffraction data. T.N. and J.T. determined and analysed the structures. T.N., S.U., Y.G., A.K. and J.T. wrote the paper.

Author Information The coordinates of $Sema6A_{SP}$, $PlxnA2_{SP}$ and their complex have been deposited in the Protein Data Bank under accession codes 3AFC, 3AL9 and 3AL8, respectively. Reprints and permissions information is available at www.nature.com/reprints. The authors declare no competing financial interests. Readers are welcome to comment on the online version of this article at www.nature.com/nature. Correspondence and requests for materials should be addressed to J.T. (takagi@protein.osaka-u.ac.jp).

METHODS

Protein expression and purification. To express the Sema6A ectodomain fragment for crystallization, a DNA fragment corresponding to residues 19–570 was amplified from mouse Sema6A cDNA[25] and fused to the C terminus of the human growth hormone (hGH) minigene using a pSGHV0 vector[27]. The resultant plasmid was stably transfected into CHO lec 3.2.8.1 cells[23], and the clone with the highest secretion level was cultured in roller bottles (Corning). A hGH–Sema6A$_{SP}$ fragment was purified from the culture supernatants by Ni-NTA agarose chromatography and treated with tobacco etch virus protease to remove the hGH portion. The cleaved Sema6A$_{SP}$ fragment was further purified by gel filtration chromatography and concentrated to ~8 mg ml^{-1} before the crystallization trials. The mouse PlxnA2$_{SP}$ fragment containing the C-terminal TARGET tag was first stably expressed using HEK293S GnT1^{-} cells and then affinity purified using P20.1-Sepharose as described previously[24].

Structure determination. Screening of crystallization conditions was performed by using mosquito (TTPLabtech). The Sema6A crystal was obtained from a solution containing 22–24% polyethylene glycol (PEG) 1500 and 0.1 M Tris-Cl pH 7.0. Cryoprotectant was prepared by mixing the reservoir solution and the ethylene glycol at a ratio of 4:1, resulting in a solution containing 20% ethylene glycol. Diffraction data were collected at Photon Factory BL-17A with an ADSC Quantum 270 CCD detector and at SPring-8 BL-41XU with a Rayonix MX225HE CCD detector, and then processed with HKL2000[28]. The crystal diffracted X-rays to 2.5 Å resolution and was found to belong to the space group $P2_1$ with unit cell dimensions of a = 71.47 Å, b = 89.06 Å, c = 95.52 Å and β = 102.2°. The initial phases were determined via the molecular replacement method with MOLREP[29], and the Sema4D structure (1OLZ) was used as a search model. Model building and refinement were performed with COOT[30] and REFMAC5[31] in which 5% of the reflections were excluded from the refinement. The crystallographic R-factor and the free R-factor were finally reduced to 21.1% and 27.8%, respectively, at 2.5 Å resolution. The quality of the final model was validated with MolProbity[32]. 95.08% of the amino acid residues were located in the favoured region of the Ramachandran plot and 0.29% were assigned as outliers.

The PlxnA2 crystal was obtained from a solution containing 24–28% PEG 3350, 0–0.2 M NaCl and 0.1 M Tris-Cl pH 8.0–8.5. Diffraction data were collected at Photon Factory BL-17A. Crystals diffracted X-rays to 2.1 Å resolution and were found to belong to the space group $P1$ with unit cell dimensions of a = 55.70 Å, b = 60.68 Å, c = 95.39 Å, α = 109.8°, β = 92.5° and γ = 112.5°. The structures of Sema3A (PDB 1Q47), Sema4D (PDB 1OLZ), Sema6A (PDB 3AFC) and the Met receptor (PDB 1SHY) were used in molecular replacement, with only the Met receptor yielding a clear solution. ARP/wARP[33] was used during the phase improvement and the crystallographic R-factor and the free R-factor were reduced to 20.5% and 25.8%, respectively, at 2.1 Å resolution. 97.56% of the residues were located in the favoured region of the Ramachandran plot and only Pro A-474 was assigned as an outlier.

The Sema6A–PlxnA2 complex crystal was obtained from a solution containing 18–25% PEG1000, 0.2–0.3 M $MgCl_2$ and 0.1 M Na Cacodylate pH 5.5–6.5, and was cryoprotected with a solution containing 25% PEG1000, 0.3 M $MgCl_2$, 0.1 M Na Cacodylate pH 6.0 and 20% ethylene glycol. Diffraction data were collected at Photon Factory BL-17A. The crystal diffracted X-rays up to 3.6 Å resolution and was found to belong to the space group $P6_122$ with unit cell dimensions of $a = b$ = 240.87 Å, c = 146.75 Å. Molecular replacement phasing was performed using the Sema6A and PlxnA2 structures. The Pt-derivative crystal for SIRAS phasing was prepared by soaking the complex crystal in a solution containing 1 mM K_2PtCl_4, 23% PEG1000, 0.2 M $MgCl_2$, and 0.1 M Na Cacodylate pH 6.0 for 24 h. The Pt-derivative crystal diffracted X-rays to 4.5 Å resolution, and the data were collected at 1.07171 Å. The phases were calculated with SHLEXC/D[34] and SHARP/autoSHARP[35] and then improved with SOLOMON[36]. The crystallographic R-factor and free R-factor were finally reduced to 23.0% and 28.7%, respectively, at 3.6 Å resolution. 90.94% of the residues were located in the favoured region of the Ramachandran plot and 0.88% were assigned as outliers. Details of the data collection and refinement statistics for Sema6A, PlxnA2 and the complex are summarized in Supplementary Tables 1, 2 and 3, respectively. The accessible surface area was calculated with AREAIMOL[37], and structural superposition was performed with SUPERPOSE[38]. Figures for the protein structures were prepared with PyMOL[39], in which electrostatic potentials were calculated with APBS[40]. For the structural details of the final models, see Supplemental Results.

Analytical ultracentrifugation. Measurements were performed with a ProteomeLab XL-I analytical ultracentrifuge (Beckman-Coulter) using An60 Ti rotor. For sedimentation velocity experiments on Sema6A$_{SP}$, runs were carried out at 42,000 r.p.m. at 20 °C using 12 mm aluminium double-sector cells loaded with various concentrations of Sema6A$_{SP}$ in buffer containing 20 mM HEPES, 150 mM NaCl, pH 7.5. For sedimentation equilibrium experiments on PlxnA2$_{SP}$, data were collected at 20 °C at 8, 16 and 48 μM in 5 mM Tris, 150 mM NaCl, pH 7.5, and at rotor speeds of 9,000, 12,000 and 15,000 r.p.m. Data were acquired with an ultraviolet absorbance detection system where appropriate wavelengths (246, 250, 258, 276, 280, 283 and 286 nm) were used depending on the concentration of the solution. Sedimentation velocity and sedimentation equilibrium data were analysed using the SEDFIT version 11.8 and SEDPHAT version 6.5 programs[41,42], respectively.

Biological assays. AP-ligand binding assays were performed as previously described[25]. To assess the biological activity of soluble Sema6A, a cell contraction assay was conducted. Briefly, HEK293T cells stably transfected with mouse PlxnA4 were seeded onto 10 mm × 10 mm glass coverslips coated with poly-L-lysine. After 24 h, the cells were incubated with varying concentrations of wild-type or M415C dimer mutant versions of Sema6A$_{SP}$ for 60 min at 37 °C. After fixing the samples with 4% paraformaldehyde in 10 mM PBS, pH 7.4 for 30 min at room temperature, the number of cells that underwent morphological changes from extended to round shapes was determined. The growth cone collapsing activity of the Sema3A–AP fusion proteins was assayed using explanted chick dorsal root ganglion (DRG) neurons as described previously[26].

27. Leahy, D. J., Dann, C. E. III, Longo, P., Perman, B. & Ramyar, K. X. A mammalian expression vector for expression and purification of secreted proteins for structural studies. *Protein Expr. Purif.* **20**, 500–506 (2000).
28. Otwinowski, Z. & Minor, W. Processing of X-ray diffraction data collected in oscillation mode. *Methods Enzymol.* **276**, 307–326 (1997).
29. Vagin, A. & Teplyakov, A. MOLREP: an automated program for molecular replacement. *J. Appl. Cryst.* **30**, 1022–1025 (1997).
30. Emsley, P. & Cowtan, K. Coot: model-building tools for molecular graphics. *Acta Crystallogr. D* **60**, 2126–2132 (2004).
31. Murshudov, G. N., Vagin, A. A. & Dodson, E. J. Refinement of macromolecular structures by the maximum-likelihood method. *Acta Crystallogr. D* **53**, 240–255 (1997).
32. Davis, I. W. *et al.* MolProbity: all-atom contacts and structure validation for proteins and nucleic acids. *Nucleic Acids Res.* **35**, W375–W383 (2007).
33. Perrakis, A., Harkiolaki, M., Wilson, K. S. & Lamzin, V. S. ARP/wARP and molecular replacement. *Acta Crystallogr. D* **57**, 1445–1450 (2001).
34. Schneider, T. R. & Sheldrick, G. M. Substructure solution with SHELXD. *Acta Crystallogr. D* **58**, 1772–1779 (2002).
35. Bricogne, G., Vonrhein, C., Flensburg, C., Schiltz, M. & Paciorek, W. Generation, representation and flow of phase information in structure determination: recent developments in and around SHARP 2.0. *Acta Crystallogr. D* **59**, 2023–2030 (2003).
36. Abrahams, J. P. & Leslie, A. G. Methods used in the structure determination of bovine mitochondrial F1 ATPase. *Acta Crystallogr. D* **52**, 30–42 (1996).
37. Lee, B. & Richards, F. M. The interpretation of protein structures: estimation of static accessibility. *J. Mol. Biol.* **55**, 379–400 (1971).
38. Krissinel, E. & Henrick, K. Secondary-structure matching (SSM), a new tool for fast protein structure alignment in three dimensions. *Acta Crystallogr. D* **60**, 2256–2268 (2004).
39. DeLano, W. L. *The PyMOL Molecular Graphics System* (DeLano Scientific, 2002).
40. Baker, N. A., Sept, D., Joseph, S., Holst, M. J. & McCammon, J. A. Electrostatics of nanosystems: application to microtubules and the ribosome. *Proc. Natl Acad. Sci. USA* **98**, 10037–10041 (2001).
41. Schuck, P. Size-distribution analysis of macromolecules by sedimentation velocity ultracentrifugation and Lamm equation modeling. *Biophys. J.* **78**, 1606–1619 (2000).
42. Schuck, P. On the analysis of protein self-association by sedimentation velocity analytical ultracentrifugation. *Anal. Biochem.* **320**, 104–124 (2003).

Biochemical and Biophysical Research Communications 402 (2010) 168–172

Contents lists available at ScienceDirect

Biochemical and Biophysical Research Communications

journal homepage: www.elsevier.com/locate/ybbrc

Th1 cells promote neurite outgrowth from cortical neurons via a mechanism dependent on semaphorins

Hiroshi Ishii [a,b], Takekazu Kubo [b], Atsushi Kumanogoh [c], Toshihide Yamashita [a,d,*]

[a] Department of Molecular Neuroscience, Graduate School of Medicine, Osaka University, 2-2 Yamadaoka, Suita, Osaka 565-0871, Japan
[b] Department of Neurobiology, Graduate School of Medicine, Chiba University, 1-8-1 Inohana, Chuoku, Chiba 260-8677, Japan
[c] Department of Immunopathology, Research Institute for Microbial Diseases, and World Premier International Immunology Frontier Research Center, Osaka University, Suita, Osaka 565-0871, Japan
[d] JST, CREST, 5, Sanbancho, Chiyodaku, Tokyo 102-0075, Japan

ARTICLE INFO

Article history:
Received 27 September 2010
Available online 12 October 2010

Keywords:
Central nervous system
Neurite outgrowth
T lymphocyte
Th1 cells

ABSTRACT

The roles of T lymphocytes in the central nervous system (CNS) are diverse; their roles in the injured CNS have been reported to be both detrimental and advantageous. Hence, an investigation of the effects of specific subsets of T cells on neurons may provide an insight into the interaction between the nervous system and the immune system. In the present study, we demonstrate that a specific subset of T lymphocytes enhanced neurite outgrowth in vitro. When cultured T helper type 1 (Th1) cells were co-cultured with cortical neurons, neurite outgrowth from neurons was enhanced; however, the same was not observed when Th2 or naïve T cells were used. We observed that the promotion of neurite outgrowth by Th1 cells was completely inhibited by anti-interferon γ (IFN-γ) neutralizing antibody, but that IFN-γ did not directly promote neurite growth. Furthermore, experiments using knockout mice revealed that semaphorin 4A (Sema4A) but not Sema7A was required for the effect produced by Th1 cells. These results demonstrate that Sema4A and IFN-γ expressed in Th1 cells play a critical role in enhancing neurite outgrowth from cortical neurons.

1. Introduction

Immune reactions after central nervous system (CNS) trauma have been thought to be harmful for axonal regeneration and functional recovery [1–3]. However, during the last decade, it has been reported that the transfer of autoimmune T cells or active immunization with T cells promoted functional recovery after CNS injury [4–9]. In contrast, others reported that T lymphocytes caused axonal damage after the CNS injury [3,10–12]. It could be assumed that these contradictory results may be explained by distinct roles of subsets of T cells such as T helper type 1 (Th1) or Th2 cells.

Subsets of helper T cells have been suggested to be involved in the etiology of CNS diseases. Interferon γ (IFN-γ)-producing Th1 cells and interleukin (IL)-17-producing helper T (Th17) cells are associated with the onset and progression of experimental autoimmune encephalomyelitis (EAE), an animal model of multiple sclerosis [13,14]. Interleukin-4-producing Th2 cells were considered to promote functional recovery after the CNS injury [15]. However, the role of each subset of T cells had not been explored in depth, and whether a specific subset of T cells was beneficial to CNS injury remained elusive. Contradictory reports on the role of T cells in vivo after a CNS injury may be because of the distinct roles of helper T cell-subsets. Hence, it is important to dissect out the precise effects of each T cell subset on neurons. For this purpose, we performed a neurite outgrowth assay using cortical neurons in vitro because this assay is considered to reveal the ability of neurons to regenerate axons in vivo. We report that Th1 cells but not Th2 cells enhanced neurite outgrowth from embryonic cortical neurons. Furthermore, we explored the molecular mechanism underlying the promotion of neurite outgrowth by Th1 cells. We investigated whether IFN-γ, which is mainly secreted by Th1 cells or semaphorins (axon guidance molecules as well as immunomodulators expressed on immune cells) [16], were required for the effects produced by Th1 cells. Our results demonstrated that Sema4A but not Sema7A was required for the effects produced by Th1 cells. Further, IFN-γ acting on Th1 cells was also required for producing these effects.

Abbreviations: CNS, central nervous system; Th1, T helper type 1; IFN-γ, interferon γ; Sema4A, semaphorin 4A; IL, interleukin; EAE, experimental autoimmune encephalomyelitis; FBS, fetal bovine serum; PBS, phosphate-buffered saline; FACS, fluorescence-activated cell sorting; BSA, bovine serum albumin; FITC, fluorescein isothiocyanate; APC, allophycocyanin.

* Corresponding author at: Department of Molecular Neuroscience, Graduate School of Medicine, Osaka University, 2-2 Yamadaoka, Suita, Osaka 565-0871, Japan. Fax: +81 6 6879 3669.
E-mail address: yamashita@molneu.med.osaka-u.ac.jp (T. Yamashita).

0006-291X/$ - see front matter © 2010 Elsevier Inc. All rights reserved.
doi:10.1016/j.bbrc.2010.10.029

2. Materials and Methods

2.1. Mice

C57BL/6 mice were purchased from Charles River. Sema7A -/- mice on the C57BL/6 background were used [17]. Sema4A -/- mice were generated as described previously [18]. All mice used in this study were housed in specific pathogen-free conditions. All the experimental procedures were approved by the Institutional Committees of Chiba University and Osaka University.

2.2. Differentiation of $CD4^+$ T cells

Spleens were collected from C57BL/6j female mice, and single-cell suspensions were prepared by mechanical disruption in RPMI-growth medium consisting of RPMI 1640 medium (Invitrogen, Carlsbad, CA) supplemented with 10% fetal bovine serum (FBS), 100 IU/ml penicillin, 100 μg/ml streptomycin, 1 μM sodium pyruvate, and 2.5 μM ß-mercaptoethanol. $CD4^+$ T cells were isolated by magnetic sorting with anti-CD4 magnetic beads according to the manufacturer's instructions (Miltenyi Biotec, Bergisch Gladbach, Germany). $CD4^+$ T cells were stimulated with anti-CD3ε antibodies (BD Biosciences, Franklin Lakes, NJ) coated on 24-well plates (Greiner Bio-One, Kremsmünster, Austria) at a concentration of 10 μg/ml. Th1 cells were differentiated by the addition of recombinant IL-2 (25 U/ml; R&D Systems, Minneapolis, MN), IL-12 (10 U/ml; R&D Systems), and anti-IL-4 antibodies (25% culture supernatant of hybridoma; clone HB-188; American Type Culture Collection, Rockville, MD). Th2 polarization was initiated by the addition of recombinant IL-2 (25 U/ml; R&D Systems), IL-4 (100 U/ml; Peprotech, Rocky Hill, NJ) and anti-IFN-γ antibodies (1% culture supernatant of hybridoma; clone CRL-1975; American Type Culture Collection). These differentiated $CD4^+$ T cells were diluted 1:3 for passage on day 2, and cultured with IL-2 and IL-12 for Th1 cells, or IL-2 and IL-4 for Th2 cells. The concentration of each cytokine used was the same as mentioned above.

2.3. Intracellular cytokine staining

Harvested $CD4^+$ T cells were stimulated for 6 hours with 2 μM monensin (Funakoshi, Tokyo, Japan) and anti-CD3ε antibodies (BD Biosciences) that were coated on 24-well plates at a concentration of 10 μg/ml for 6 hours. After washing the cells twice with cold phosphate-buffered saline (PBS), the T cells were fixed with 4% (wt/vol) paraformaldehyde for 10 minutes at room temperature. The cells were then washed twice with fluorescence-activated cell sorting (FACS) buffer (1% bovine serum albumin (BSA) in PBS) and permeabilized with permeabilization buffer (50 mM NaCl, 5 mM EDTA, 0.02% NaN_3, 0.5 % Triton X; pH 7.5) for 10 minutes on ice. After washing the cells twice with FACS buffer, the cells were blocked with 3% BSA in PBS for 15 minutes on ice. The cells were again washed with FACS buffer, and subjected to intracellular staining using anti-IFN-γ-fluorescein isothiocyanate (FITC) and anti-IL-4- allophycocyanin (APC) antibodies (BD Biosciences).

2.4. FACS analysis

FACS analysis was performed on a FACSCaliber (BD Biosciences) and analyzed using ProQuest software (BD Biosciences).

2.5. Co-culture of neurons and lymphocytes

Cortical neurons from the cerebral cortex were obtained from mice on embryonic day 15 and 16; they were dissociated by trypsinization (0.25% trypsin in PBS for 15 min at 37 °C), resuspended in a serum-containing medium, triturated, and washed 3 times with PBS. The dissociated neurons were plated at 1.5×10^4 cells/cm^2 into Lab-Tek 4-well chamber slides (Thermo Fisher Scientific, Waltham, MA) coated with poly-l-lysine in serum-free Neuro-basal medium (200 μl per well; Invitrogen) supplemented with B27 (Invitrogen), and l-glutamine (Nacalai Tesque, Kyoto, Japan). Cultured Th1/Th2 $CD4^+$ T cells were diluted 1:2 on day 4, and cultured for 1 day with IL-2 (25 U/ml) and IL-12 (10 U/ml) for Th1 cells, and IL-2 (25 U/ml) and IL-4 (100 U/ml) for Th2 cells. These cells were harvested on day 5 and plated (1.5×10^4 cells/cm^2) with 200 μl conditioned RPMI-growth medium per well in chamber slides containing cortical neurons. $CD4^+$ T cells isolated by magnetic sorting with anti-CD4 magnetic beads were used as naïve helper T cells. The cortical neurons and the T cells were co-cultured for 24 hours. As control, 200 μl RPMI-growth medium lacking the cells was added to a chamber in which cortical neurons were plated. Where indicated, recombinant IFN-γ (20 ng/ml; R&D) was added in the culture medium of the cortical neurons. In addition, anti-IFN-γ antibodies (1% culture supernatant of hybridoma; clone CRL-1975; American Type Culture Collection) were added into the co-culture 1 hour prior to the addition of T cells into the neuronal culture. Th1-conditioned cells (in the presence of IL-12 plus anti-IL-4) were differentiated from $CD4^+$ T cells derived from spleens of semaphorin-knockout mice according to the same protocol as mentioned above. Sema7A (-/-) and Sema4A (-/-) mice were used.

2.6. Measurement of neurite length from cortical neurons

The co-cultured neurons were fixed in 4% (wt/vol) paraformaldehyde and immunostained with a monoclonal antibody (TuJ1) that recognized the neuron-specific ß tubulin III protein (1:1000; Covance, Princeton, NJ). The neurons were viewed under an inverted light microscope equipped with epifluorescence optics

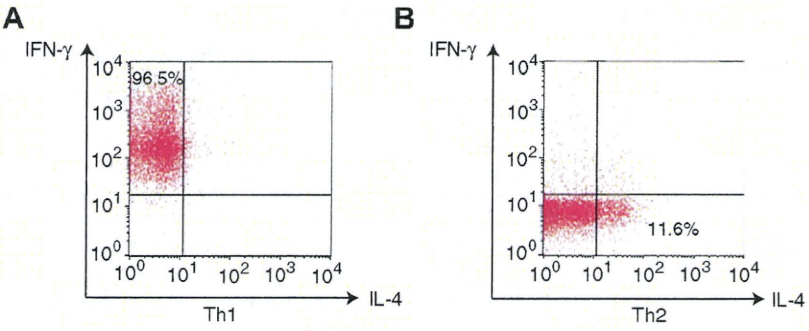

Fig. 1. Isolated naïve $CD4^+$ T cells differentiated into Th1 and Th2 cells. (A) Representative dot plots of FACS analysis. Most of the cultured $CD4^+$ T cells, which were treated with IL-2, IL-12, and anti-IL-4 antibodies, secreted IFN-γ; this is a distinct characteristic of differentiated Th1 cells. (B) Cultured $CD4^+$ T cells treated with IL-2 and IL-12 secreted IL-4 that is a distinct characteristic of differentiated Th2 cells.

and a dry condenser for phase-contrast microscopy (DP70, Olympus). The length of the longest neurite was measured for each TuJ1-positive neuron using ImageJ (National Institutes of Health, USA). In each set of experiments, more than 80 neurites were measured, and their mean length was calculated.

3. Results

3.1. Cultured Th1 cells enhance neurite outgrowth

In order to assess the functional interaction between neurons in the CNS and T cells, we performed a neurite growth assay. We examined neurite outgrowth from cortical neurons in the cerebral cortex of mice on embryonic day 15 and 16 for 24 hours. The effect of helper T cells on the neurons was examined by co-culture. For this experiment, $CD4^+$ naïve helper T cells isolated ex vivo from mice spleens between postnatal weeks 7 and 9 were differentiated into Th1 or Th2 cells. First, we confirmed successful differentiation of the $CD4^+$ naïve helper T cells into Th1 (Fig. 1A) or Th2 (Fig. 1B) cells by quantifying the amount of IFN-γ and IL-4 with FACS analysis. The differentiated helper T cells were then added to the neuron culture (Fig. 2, schematic figure on top). After 24 hours, these co-cultured cells were fixed, and immunostained with the monoclonal antibody (TuJ1) that recognizes the neuron-specific ß tubulin III protein in order to label the neurites of neurons. Neurite outgrowth from the cortical neurons was significantly boosted when the neurons were co-cultured with Th1 cells as compared to that observed in the controls (Fig. 2A and B). Naïve helper T cells or Th2 cells did not modulate the neurite growth rate (Fig. 2A and B). The mean neurite length of the cortical neurons maintained without co-culture (RPMI-growth medium was used in a control) and of those co-cultured with naïve helper T cells, and of Th1 or Th2 cells was 54.6 μm, 60.2 μm, 73.1 μm, and 55.2 μm, respectively. Therefore, Th1 cells but not naïve helper T cells or Th2 cells promoted neurite growth from the cortical neurons in vitro.

3.2. IFN-γ is associated with the promotion of neurite outgrowth by Th1 cells

Next, we tried to explore the molecular mechanism underlying the promotion of neurite elongation by Th1 cells. We first investigated whether IFN-γ, which is one of the major cytokines secreted from Th1 cells, directly acted on the cortical neurons to promote neurite outgrowth. To test this hypothesis, we treated the cortical neurons with recombinant IFN-γ at a concentration of 20 ng/ml, and measured neurite growth. However, IFN-γ appeared to inhibit neurite growth (Fig. 3). This result excludes the possibility that IFN-γ secreted by Th1 cells acted directly on the neurons to enhance neurite elongation. Then, we determined whether endogenous IFN-γ acted on Th1 cells in an autocrine manner and indirectly produced the effect on neurons. For this purpose, anti-IFN-γ neutralizing antibody was added to the co-culture. Interestingly, we observed that the promotion of neurite outgrowth by Th1 cells was completely diminished after treatment with the anti-IFN-γ neutralizing antibody (Fig. 3). These results demonstrate that the effect of IFN-γ on Th1 cells was necessary for the promotion of neurite growth by Th1 cells. IFN-γ may act on Th1 cells but not on the neurons, thereby resulting in enhanced neurite growth. Other factors secreted by the Th1 cells may be responsible for the effect produced by the Th1 cells on neurons.

3.3. Sema4A but not Sema7A is required for Th1 cell-enhanced neurite outgrowth

To identify the molecules secreted from Th1 cells, we focused on semaphorin family members. Semaphorin family of membrane

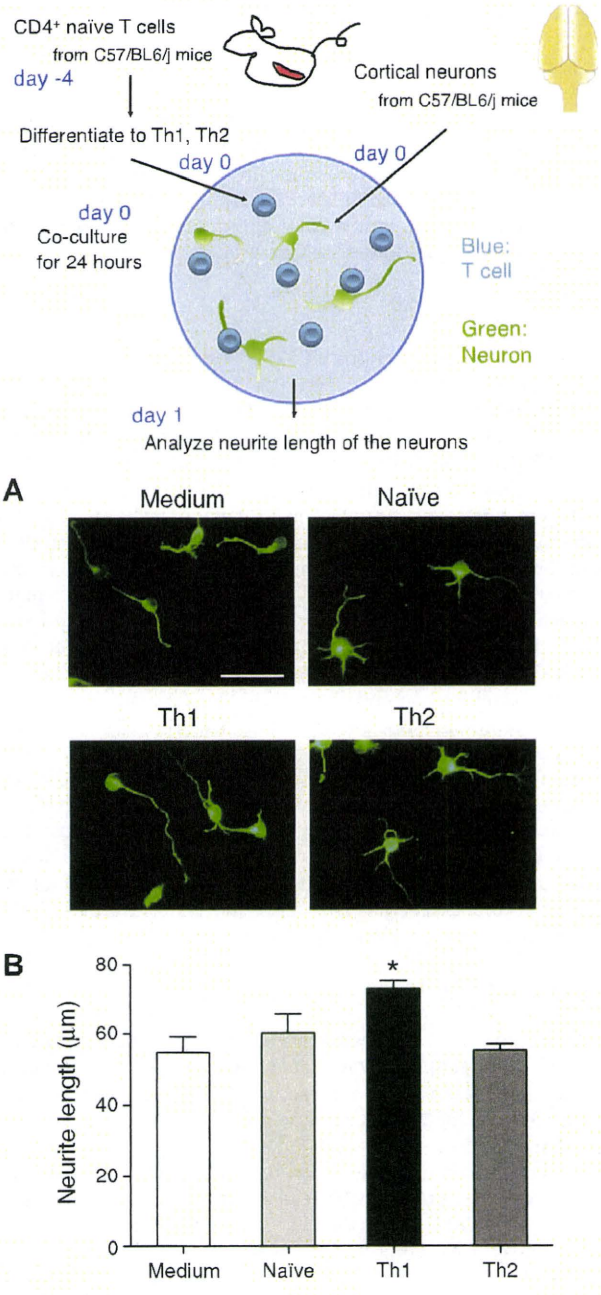

Fig. 2. Cultured Th1 cells but not Th2 cells promoted neurite outgrowth from cortical neurons in vitro. (Upper panel) Schematic figure indicating the protocol for the co-culture of helper T cells and cortical neurons. (A) Representative images of Tuj1-labeled neurons. Scale bar = 50 μm (B) Quantification of neurite length after co-culture for 24 hours. Medium: Control, n = 4; Naïve, n = 4; Th1, n = 4; Th2, n = 4. Values are the mean (SEM) $^*P < 0.05$ versus control group (one-way ANOVA with Dunnett's post-test).

proteins plays a role in not only axon guidance of developing neurons but also modulation of the immune system [16]. Among the family members, Sema7A was reported to be expressed in T cells [19] and promote axon growth in olfactory neurons [17]. We obtained T cells derived from spleens of Sema7A-knockout mice, and induced differentiation of these cells in the presence of IL-12 plus anti-IL-4 (Th1-skewing conditions). The results demonstrated that Th1-conditioned cells lacking Sema7A promoted neurite growth to the same extent as Th1 cells from wild-type mice (Fig. 3). Hence, it was inferred that Sema7A was not required for

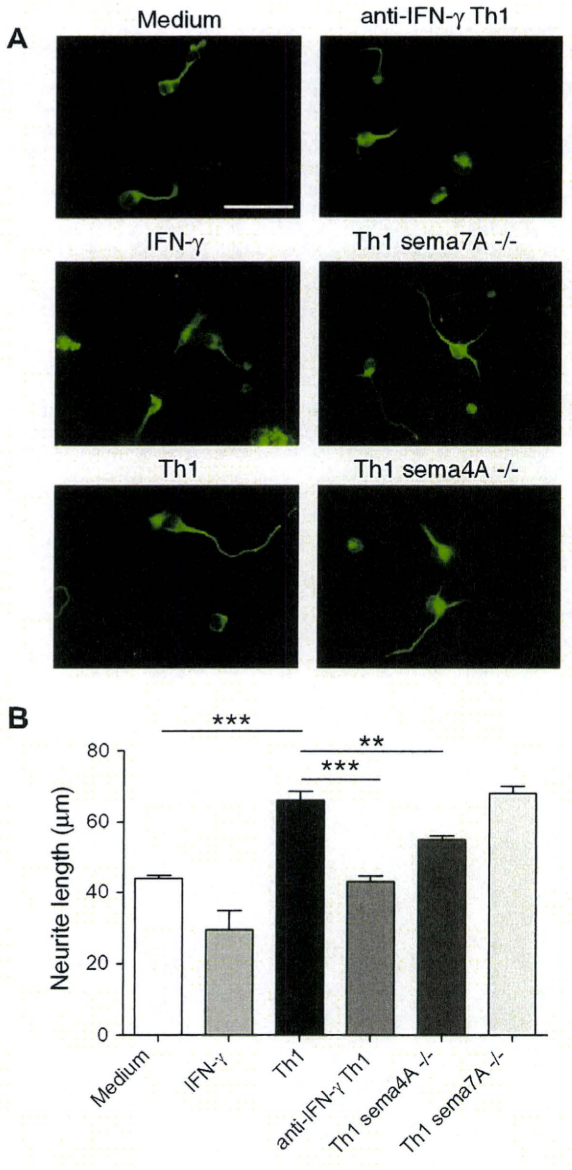

Fig. 3. Th1 cells required IFN-γ and Sema4A for the promotion of neurite outgrowth. (A) Representative images of Tuj1-labeled neurons. Scale bar = 50 μm (B) Measurement of neurite length after 24-hour culture of the cortical neurons. Recombinant IFN-γ or neutralizing antibody to IFN-γ was added to the culture medium. Th1-conditioned cells were differentiated from $CD4^+$ T cells derived from spleens of wild-type, Sema7A -/-, or Sema4A -/- mice, and added into the neuronal culture. Medium: Control, n = 4; IFN-γ, n = 2; Th1, n = 4, anti-IFN-γ: IFN-γ-neutralizing antibodies, n = 3; Th1 Sema4A -/-, n = 4; Th1 sema7A -/-, n = 3. Values are the mean (SEM) $^{**}P < 0.01$, $^{***}P < 0.001$ (one-way ANOVA with Bonferroni's post-test).

producing the effect of Th1 cells on neurons. Finally, we examined whether Sema4A, another member of the semaphorin family, was involved in producing the effect of Th1 cells because Sema4A is also expressed in T cells [20] and induces growth cone collapse of hippocampal neurons [21]. The neurite growth-promoting effect of Th1-conditioned cells lacking Sema4A was significantly lower than that of wild-type Th1 cells (Fig. 3). These results demonstrate that Sema4A is necessary for the effects of cultured Th1 cells. However, it should be noted that the effect of Th1 cells was not completely abolished when Th1-conditioned cells lacking Sema4A were used. Therefore, other molecules such as neurotrophic factors may also play an additional role in promoting neurite growth from cortical neurons.

4. Discussion

There have been controversies concerning the efficacy of adoptive transfer of T lymphocytes during CNS trauma [15]. Critically, no experiments focusing on specific T cell subsets with regard to these conflicting results have been reported. In the present study, we investigated the effects of specific T cell subsets on neurite outgrowth to evaluate neuronal regeneration in vitro. Unexpectedly, Th1 cells, which were suggested to be detrimental during CNS injury [15] and pathogenic during EAE [13,14], enhanced neurite outgrowth from cerebral cortical neurons, although naïve helper T cells or Th2 cells did not have such effects. These results are seemingly inconsistent with a previously reported hypothesis [15]. However, IFN-γ that is dominantly secreted from Th1 cells was reported to enhance neurogenesis in the brain [22] and be protective in EAE [23]. Indeed, we identified that IFN-γ was required by Th1 cells for enhancing neurite outgrowth, although IFN-γ itself appeared to act on Th1 cells but not on the neurons directly. In addition, experiments with cultured T cells derived from Sema4A-knockout mice revealed that Sema4A in Th1 cells was required by Th1 cells for promoting neurite outgrowth. Because Sema4A is a membrane-spanning molecule that differs from the secretory cytokine IFN-γ, it is possible that there was direct interaction between Th1 cells and the cortical neurons, and thus the Sema4A signal was transduced to the cortical neurons. However, it was reported that Sema4A induced growth cone collapse of other types of neurons, including hippocampal neurons [21]. Thus, the function of Sema4A in the CNS may be cell context dependent. Another possibility is that Th1-conditioned cells lacking Sema4A may secrete trophic factors at a lower level than wild-type Th1 cells because of the defective T cell differentiation. Because the production of IFN-γ by Th1-conditioned cells from Sema4A-deficient mice was severely impaired compared to that in wild-type mice [18], it is also likely that the reduction of IFN-γ due to the absence of Sema4A leads to the attenuation of enhanced neurite growth by Th1 cells.

In accordance with our results, it could be assumed that the reported beneficial effects of T cells transferred into animals after CNS injury may be attributed to the Th1 subset. Inconsistent results obtained in vivo could be explained by the diversity in the ratio of specific subsets of T cells. Therefore, the precise in vivo role of specific subsets of T cells should be determined, presumably by the transfer of each subset of the T cells. This topic should be explored in future studies.

Acknowledgments

We thank Dr. T. Nakayama, Dr. M. Yamashita, and Dr. M. Kuwahara at Chiba University for their technical advice on T cell-culture. This work was supported by a research grant from a Grant-in-Aid (S) from Ministry of Health, Labour and Welfare.

References

[1] Y. Taoka, K. Okajima, M. Uchiba, et al., Role of neutrophils in spinal cord injury in the rat, Neuroscience 79 (1997) 1177–1182.
[2] C. Profyris, S.S. Cheema, D. Zang, et al., Degenerative and regenerative mechanisms governing spinal cord injury, Neurobiol. Dis. 15 (2004) 415–436.
[3] J.R. Potas, Y. Zheng, C. Moussa, et al., Augmented locomotor recovery after spinal cord injury in the athymic nude rat, J. Neurotrauma 23 (2006) 660–673.
[4] G. Moalem, R. Leibowitz-Amit, E. Yoles, et al., Autoimmune T cells protect neurons from secondary degeneration after central nervous system axotomy, Nat. Med. 5 (1999) 49–55.
[5] H. Hammarberg, O. Lidman, C. Lundberg, et al., Neuroprotection by encephalomyelitis: rescue of mechanically injured neurons and neurotrophin production by CNS-infiltrating T and natural killer cells, J. Neurosci. 20 (2000) 5283–5291.
[6] E. Hauben, O. Butovsky, U. Nevo, et al., Passive or active immunization with myelin basic protein promotes recovery from spinal cord contusion, J. Neurosci. 20 (2000) 6421–6430.

[7] E. Yoles, E. Hauben, O. Palgi, et al., Protective autoimmunity is a physiological response to CNS trauma, J. Neurosci. 21 (2001) 3740–3748.
[8] J. Kipnis, T. Mizrahi, E. Hauben, et al., Neuroprotective autoimmunity: naturally occurring CD4+CD25+ regulatory T cells suppress the ability to withstand injury to the central nervous system, Proc. Natl. Acad. Sci. U S A 99 (2002) 15620–15625.
[9] H.H. Hofstetter, D.L. Sewell, F. Liu, et al., Autoreactive T cells promote post-traumatic healing in the central nervous system, J. Neuroimmunol. 134 (2003) 25–34.
[10] U. Gimsa, S.V. Peter, K. Lehmann, et al., Axonal damage induced by invading T cells in organotypic central nervous system tissue in vitro: involvement of microglial cells, Brain Pathol. 10 (2000) 365–377.
[11] D. Fee, A. Crumbaugh, T. Jacques, et al., Activated/effector CD4+ T cells exacerbate acute damage in the central nervous system following traumatic injury, J. Neuroimmunol. 136 (2003) 54–66.
[12] T.B. Jones, D.P. Ankeny, Z. Guan, et al., Passive or active immunization with myelin basic protein impairs neurological function and exacerbates neuropathology after spinal cord injury in rats, J. Neurosci. 24 (2004) 3752–3761.
[13] H. Kebir, K. Kreymborg, I. Ifergan, et al., Human TH17 lymphocytes promote blood-brain barrier disruption and central nervous system inflammation, Nat. Med. 13 (2007) 1173–1175.
[14] R.A. O'Connor, C.T. Prendergast, C.A. Sabatos, et al., Cutting edge: Th1 cells facilitate the entry of Th17 cells to the central nervous system during experimental autoimmune encephalomyelitis, J. Immunol. 181 (2008) 3750–3754.
[15] S. Hendrix, R. Nitsch, The role of T helper cells in neuroprotection and regeneration, J. Neuroimmunol. 184 (2007) 100–112.
[16] A. Kumanogoh, H. Kikutani, Immune semaphorins: a new area of semaphorin research, J. Cell Science 116 (2003) 3463–3470.
[17] R.J. Pasterkamp, J.J. Peschon, M.K. Spriggs, et al., Semaphorin 7A promotes axon outgrowth through integrins and MAPKs, Nature 424 (2003) 398–405.
[18] A. Kumanogoh, T. Shikina, K. Suzuki, et al., Nonredundant roles of Sema4A in the immune system: defective T cell priming and Th1/Th2 regulation in Sema4A-deficient mice, Immunity 22 (2005) 305–316.
[19] T. Mine, K. Harada, T. Matsumoto, et al., CDw108 expression during T-cell development, Tissue Antigens 55 (2000) 429–436.
[20] A. Kumanogoh, S. Marukawa, K. Suzuki, et al., Class IV semaphorin Sema4A enhances T-cell activation and interacts with Tim-2, Nature 419 (2002) 629–633.
[21] K. Yukawa, T. Tanaka, T. Bai, et al., Semaphorin 4A induces growth cone collapse of hippocampal neurons in a Rho/Rho-kinase-dependent manner, Int. J. Mol. Med. 16 (2005) 115–118.
[22] R. Baron, A. Nemirovsky, I. Harpaz, et al., IFN-gamma enhances neurogenesis in wild-type mice and in a mouse model of Alzheimer's disease, FASEB J. 22 (2008) 2843–2852.
[23] S. Pastor, A. Minguela, W. Mi, et al., Autoantigen immunization at different sites reveals a role for anti-inflammatory effects of IFN-gamma in regulating susceptibility to experimental autoimmune encephalomyelitis, J. Immunol. 182 (2009) 5268–5275.